Brigham Young University
BYU ScholarsArchive

Theses and Dissertations

2021-01-07

Sp2 Bonded Carbon for Soft X-Ray Detector Windows

Joseph T. Rowley
Brigham Young University

Follow this and additional works at: https://scholarsarchive.byu.edu/etd

Part of the Physical Sciences and Mathematics Commons

BYU ScholarsArchive Citation
Rowley, Joseph T., "Sp2 Bonded Carbon for Soft X-Ray Detector Windows" (2021). *Theses and Dissertations*. 9365.
https://scholarsarchive.byu.edu/etd/9365

This Dissertation is brought to you for free and open access by BYU ScholarsArchive. It has been accepted for inclusion in Theses and Dissertations by an authorized administrator of BYU ScholarsArchive. For more information, please contact ellen_amatangelo@byu.edu.

Sp^2 Bonded Carbon for Soft X-Ray Detector Windows

Joseph T. Rowley

A dissertation submitted to the faculty of
Brigham Young University
in partial fulfillment of the requirements for the degree of

Doctor of Philosophy

Robert C. Davis, Chair
Richard R. Vanfleet
David D. Allred
Brian D. Jensen
Eric R. Homer
Sterling Cornaby

Department of Physics and Astronomy

Brigham Young University

Copyright © 2020 Joseph T. Rowley

All Rights Reserved

ABSTRACT

Sp^2 Bonded Carbon for Soft X-Ray Detector Windows

Joseph T. Rowley
Department of Physics and Astronomy, BYU
Doctor of Philosophy

Energy Dispersive X-Ray Spectroscopy (EDS) is a technique used to analyze materials to determine their elemental makeup. This technique is used extensively in the semiconductor industry, metallurgical industry, biology, chemistry, materials science, and other fields.

EDS detectors are often attached to scanning electron microscopes (SEM) or transmission electron microscopes (TEM) and are actively cooled by liquid nitrogen or Peltier devices. A thin membrane, or window, is fitted to the front of the detector which allows for an airtight seal as well as transmission of x-rays. The challenge for these windows is maximizing the transmission of x-rays while maintaining mechanical integrity.

Carbon is an element with a low atomic number and has several allotropes that have attributes desirable for an x-ray window. Amorphous carbon has good chemical resistance as well as being able to be sputtered, a low temperature process. Sputtered amorphous carbon is characterized in this work, including sputtered amorphous carbon that is used as part of x-ray windows. Part of this characterization involved using bulge testing. A bulge testing device was created at BYU and this is presented here. Additionally, this device was used to characterize thin films as part of this work.

Graphene is a single layer of sp^2 bonded carbon atoms in a plane. It is one of the stiffest materials known, as well as having an extremely high tensile strength (> 200 times steel). Single layer graphene has not been able to span the dimensions needed for use in a detector window, but many-layer graphene (MLG, a film with > 10 stacked layers of graphene) has been shown to span mm size openings. Many-layer graphene films were grown using chemical vapor deposition (CVD) on nickel substrates and suspended over different sized openings as well as on a silicon support structure. A description of synthesis and characterization of these films are presented here. Also presented is additional work to improve the fabrication of these MLG films by developing improved nickel substrate surfaces.

Keywords: carbon, graphene, EDS

ACKNOWLEDGEMENTS

I would like to acknowledge Moxtek, Inc., Orem, Utah for their support of this project. Their funding made this possible, and the expertise shared by their talented team of engineers and scientists, specifically Sterling Cornaby, Jonathan Abbott, Richard Creighton, and Malorie Harker contributed greatly to the success of this work. Dr. Davis has been an excellent advisor, helping me learn the complexities of experimental research while also being supportive of my needs as well as the needs of my family. He was a critical help for me and opened up this great opportunity to study at BYU. Dr. Vanfleet and Dr. Allred also taught me many things about microanalysis and characterization of thin films. I sincerely appreciate their help. I would also like to thank the wonderful staff in the Department of Physics and Astronomy at BYU. Shelena Shamo and Nan Ah You were critical in helping me understand and manage all the administrative tasks necessary for this work.

I would like to thank my family. My loving wife Lauren has supported me throughout this process and been a great strength to me. Also, I want to thank my children who have been patient and supportive of me as well. I am grateful to my father who inspired me at a young age with the wonders of technology and the universe, and my mother who always supported me.

Table of Contents

Sp^2 Bonded Carbon for Soft X-Ray Detector Windows i

ABSTRACT ii

ACKNOWLEDGEMENTS iii

Table of Contents iv

LIST OF TABLES viii

LIST OF FIGURES ix

Chapter 1 Introduction 1

1.1 Energy Dispersive Spectroscopy 1

1.1.1 Brief History 1

1.1.2 EDS Devices 2

1.2 Micro and Nanoscale Film Fabrication Techniques 5

1.2.1 Sputtering 5

1.2.2 Chemical Vapor Deposition 7

1.2.3 Spin-coating 7

1.2.4 Photolithography and Reactive Ion Etching 8

1.3 Characterization Techniques 9

1.3.1 Atomic Force Microscopy 10

1.3.2 Stress and Stress Measurement. 10

1.3.3 Scanning Electron Microscope 11

1.3.4 Transmission Electron Microscope 12

1.3.5 X-Ray Diffraction 12

1.3.6 Raman Spectroscopy 13

1.3.7 Bulge Testing 13

1.4 Scope of Work 13

Chapter 2 Sputtered Carbon as a Corrosion Barrier for X-Ray Detector Windows 16

2.1 Introduction 16

2.2 Experimental 20

2.2.1 Hydrogenated Amorphous Carbon Reactive Sputtering 20

2.2.2 Corrosion Resistance Testing 20

2.2.3 Intrinsic Stress Measurement 20

2.2.4 EELS 21

2.2.5 Raman Spectroscopy 21

2.2.6 Bulge Testing for Determination of Modulus and Strength 21

2.2.7 CHN Elemental Analysis 22

2.3 Results 22

2.4 Discussion 27

Chapter 3 Automated Burst Tester of Large Diameter Samples over a Large Pressure Range With Displacement Measurement 29

3.1 Introduction 29

3.2 Bulge Tester Design 29

3.3 Bulge Testing a Simple Membrane: Silicon Nitride 31

3.4 Bulge Testing Wrinkled, Relatively Thick Membranes: Aluminum and Copper Foils 33

3.5 Conclusion 37

Chapter 4 Uniformity of Suspended Many-layer Graphene Membranes: Impact of Nickel Foil Thickness and Surface Microtexturing 38

4.1 Introduction 38

4.2 Experimental Methods 40

4.2.1 Nickel foil polishing 40

4.2.2 Chemical Vapor Growth of MLG Film 41

4.2.3 MLG Film Transfer to Silicon Support Structures 41

4.2.4 Atomic Force Microscopy 42

4.2.5 Raman Spectroscopy 43

4.2.6 X-Ray Transmission 43

4.2.7 Optical Imaging 43

4.2.8 Burst Testing 43

4.3 Results 44

4.3.1 Ni Foil Results 44

4.3.2 MLG Films Results 46

4.4 Discussion 53

4.5 Conclusion 55

Chapter 5 Brief Preliminary Studies 57

5.1 Alternate Formation Methods for Many-layer Graphene Films 57

5.1.1 Templated Growth 58

5.1.2 Single Crystal Ni 63

Chapter 6 Conclusion and Future Work 66

Bibliography 70

LIST OF TABLES

Table 2.1 Thickness, stress and sp^3/sp^2 ratio data for sputtered carbon films 23

Table 3.1 Calculated mechanical properties of metal foils.. 35

Table 4.1 Summary of thickness results from optical transmission testing................................. 51

LIST OF FIGURES

Figure 1.1 Schematic of energy dispersive spectroscopy principle. 1

Figure 1.2 Schematic of Si(Li) detector.. 3

Figure 1.3 Schematic of sputtering process 6

Figure 1.4 Schematic of Chemical Vapor Deposition Process 7

Figure 1.5 Schematic of photolithography and reactive ion etch process 9

Figure 2.1 Comparison of a polymer supported aluminum thin film used in an x-ray detector window with and without a carbon corrosion barrier 17

Figure 2.2 Transmission optical micrographs of an aluminum thin film deposited on a polymer membrane and subjected to corrosion testing 23

Figure 2.3 EELS characterization of chemical bonding 25

Figure 2.4 Normalized Raman spectra of carbon sputtered with (10% ethylene in argon) and without (argon only) reactive gas 26

Figure 2.5 Pressure vs. displacement for an amorphous carbon suspended film 27

Figure 3.1 Cross section and 3D render of bulge test device.. 31

Figure 3.2 Displacement profiles of a 500 nm thick silicon nitride membrane suspended over a circular hole of diameter 7 mm 33

Figure 3.3 Height profiles of a 25µm thick aluminum foil sample suspended over a 4 by 24 mm rectangular hole.. 35

Figure 4.1 Transfer process for MLG on nickel foil.. 42

Figure 4.2 AFM characterization of nickel foil growth substrate... 45

Figure 4.3 Optical transmission through MLG film suspended on a ribbed x-ray window support structure........ 46
Figure 4.4 Raman Characterization of MLG film 47
Figure 4.5 Optical transmission micrographs of MLG films suspended over rectangular holes in silicon........ 49
Figure 4.6 MLG film statistics box plots........ 50
Figure 4.7 X-ray transmission of MLG film and comparison materials........ 51
Figure 4.8 Burst pressure of suspended MLG films........ 53
Figure 5.1 Images of MLG film as it was bulge tested........ 58
Figure 5.2 TEM image of multiwalled carbon nanotube........ 59
Figure 5.3 SEM image of carbon film growth on top of single layer graphene........ 60
Figure 5.4 EDS spectra of carbon film, inset is region of film that cracked........ 60
Figure 5.5 Cross section of carbon film growth on top of single layer graphene........ 61
Figure 5.6 Raman spectra from carbon film grown on single layer graphene........ 62
Figure 5.7 Raman Spectra from a single layer graphene sample on Si substrate before and after heating in hydrogen environment........ 63
Figure 5.8 Modified DV-602A Sputtering system........ 64
Figure 5.9 OIM image of MgO substrate after etching Ni/Cu films........ 65

Chapter 1 Introduction

1.1 Energy Dispersive Spectroscopy

Energy Dispersive Spectroscopy (EDS) is a technique for chemical analysis that determines a qualitative and sometimes quantitative elemental composition of a solid sample. Electrons are accelerated into a localized area (μm's or nm's) to excite electrons from the lowest energy states in the atom. This causes electrons from higher energy states to drop down into lower energy states, emitting an x-ray (Figure 1.1).

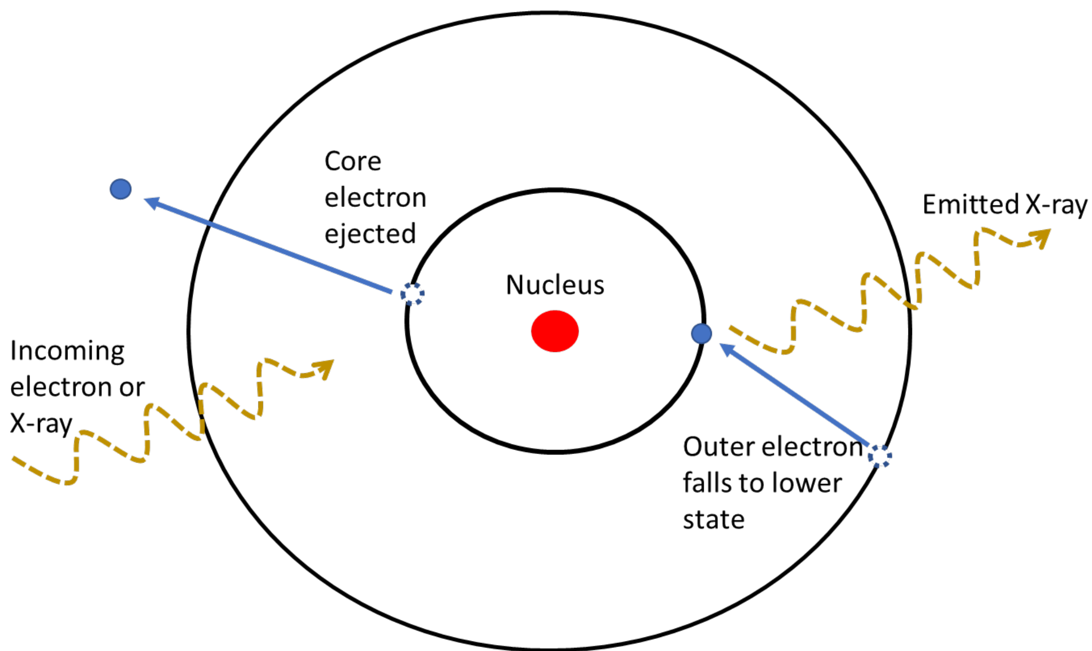

Figure 1.1 Schematic of energy dispersive spectroscopy principle.

1.1.1 Brief History

Goldstein et al. present a brief history of localized elemental analysis of solid samples in electron microscopy[1]. Hillier patented the concept of using a spectroscope to analyze x-rays

emitted from samples that were excited using an electron beam[2]. Several devices were invented to follow the initial ideas of this electron probe microanalyzer (EPMA). At first, a microscope using visible light was used to align the area of interest, and a wavelength-dispersive spectrometer (WDS) was then used to analyze the x-rays emitted by the sample. The WDS systems would use a crystal to disperse the x-rays so a narrow energy range could be focused on a detector that would measure the intensity of the x-ray radiation. Later, Cosslett and Duncumb[3] built a scanning EPMA, using a raster technique like current SEMs. Fitzgerald et al.[4] would then couple an EDS system with an EPMA.

1.1.2 EDS Devices

The x-ray detector used by Fitzgerald was based on a lithium-drifted silicon, or Si(Li) detector. This type of detector functions basically as one large p-i-n junction. A Si atom has 4 valence electrons and will bond with 4 Si neighbors when it forms a solid. Because of this, Si will have a full valence band and an empty conduction band, and no excess holes or electrons for conduction. When a photon of sufficient energy is absorbed, an electron from the valence band can be promoted to the conduction band, and Si can then conduct current. Intrinsic silicon is not reasonable to produce and thus a suitable substitute can be made using lithium doping of p-type silicon. Lithium is diffused into p-type silicon at an elevated temperature to create an intrinsic region, and an electric field drives the Li further, creating an intrinsic region that is millimeters thick. Lithium is mobile in silicon even at room temperature, and if a bias were applied the lithium would quickly diffuse to one side of the device, destroying the intrinsic region. Even storing detectors under no bias for extended periods of time degrades performance[5, 6]. In operation the device is cooled to liquid nitrogen temperatures. To apply a bias and read out the current, contacts are attached to the p-type and n-type edges of the detector. The contact in front

of the detector, as well as the region in front of the intrinsic region (typically referred to as dead silicon) will block some x-rays.

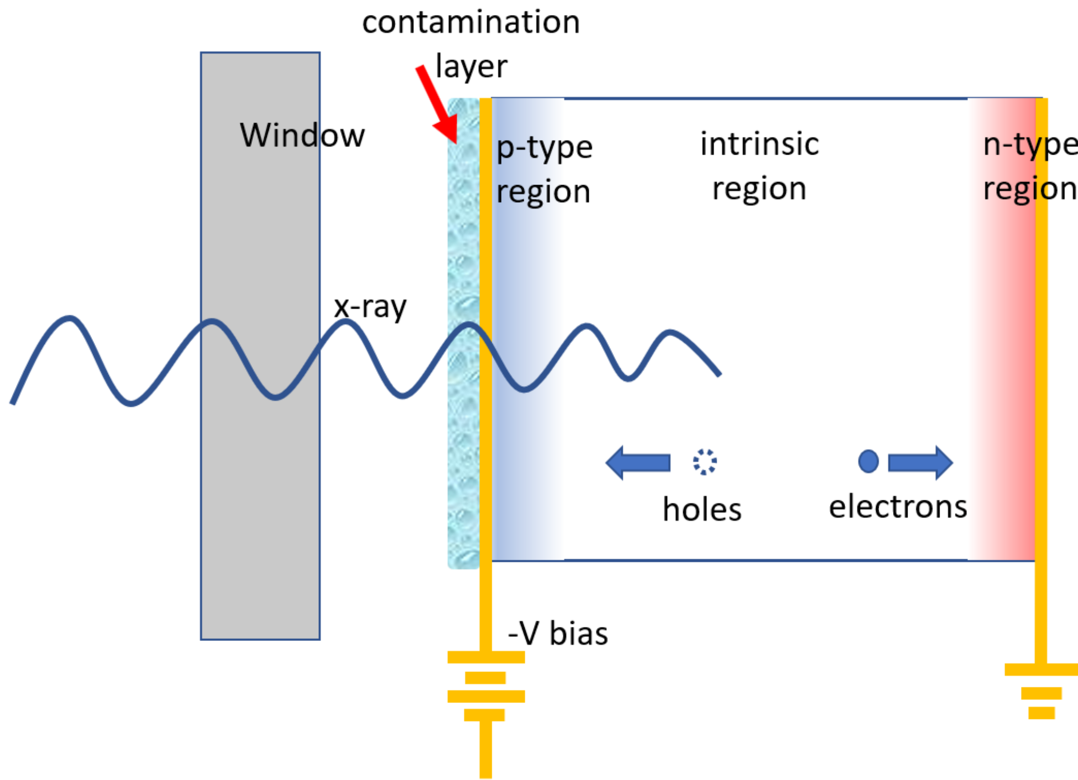

Figure 1.2 Schematic of Si(Li) detector

Silicon drift detectors[7] are devices used for x-ray detection that are similar to CCDs, or charge coupled devices. An n-type substrate as used with p-type concentric rings on the backside and a collecting anode in the center. The bias on the p-type concentric rings increases as they approach the central anode. This way an electric field parallel to the surface can drive charges to the collecting anode. This device does not need to be cooled to as low a temperature as Si(Li) devices and does not need contacts or a dead silicon area in front of the active detection volume.

An x-ray detector that is cooled will collect material on the surface (Figure 1.2). This material that builds up will interfere with x-ray detection and analysis. Therefore, as samples are

introduced and removed for analysis in an electron microscope, it is important that the detector be sealed off in a vacuum environment. However, there must be a window to allow the entry of x-rays into the detector. This window must be robust enough to withstand the changes in pressure as the environment cycles between vacuum and atmospheric pressure as samples are exchanged.

An x-ray detector window must be thin, strong, and impermeable to gases. These qualities are often at odds with each other. The thinner the film, the better the x-ray transmission, however, the strength decreases, and the permeability usually increases. Generally, x-ray transmission increases the lower an element's atomic number[8]. Materials made from low atomic number elements that can be made into thin strong films are essential for x-ray windows.

Beryllium foils have been the standard for high transmission with good vacuum compatibility. Beryllium has a low atomic number, high strength and modulus, and low permeability. However, beryllium particles are extremely hazardous when inhaled, and often it is difficult to obtain a good supply of raw material, thus there is a strong incentive for alternatives. Elements with lower weight are lithium, helium, and hydrogen. Helium and hydrogen are gases at room temperature and lithium is highly reactive. Thus, alternatives to beryllium will most likely be made from elements that have a higher atomic weight and transmit fewer x-rays (although hydrogen and lithium can be incorporated into a wide array of compounds). Current state of the art windows are made of a thin polymer film and other materials on top of a mechanical support grid. To block visible light, and to maintain an airtight seal, the window also contains a thin-film metal layer. The metal layer is protected by a thin amorphous carbon coating to maintain the metal's integrity. This carbon coating will be discussed further in Chapter 2.

Because carbon is also an element with a low atomic number it is a good candidate for x-ray detector windows if a suitable form has sufficient strength. The amorphous carbon coating for metallic films in x-ray windows work well for protecting a metal surface but lack the mechanical strength to function as an x-ray window on its own. Graphene is a form of carbon that has shown high mechanical strength and the ability to form an airtight seal. Graphene is a single layer of sp^2 bonded carbon elements in a plane. This single layer of graphene has a high specific strength but is insufficient to span support structure dimensions. Many-layer graphene films, or films made from 10 or more layers of graphene stacked on top of each other, have demonstrated the ability to span dimensions on the order of millimeters. Because these films are still less than one micron thick, and have shown the ability to span large diameters, these films fit several of the conditions needed to make high performance x-ray windows.

1.2 Micro and Nanoscale Film Fabrication Techniques

Thin films are used in the construction of x-ray windows and their deposition and growth use many of the same methods that are common in the semiconductor industry. A very brief description of these techniques will be given here. For further information on these thin film processes, the book by Ohring provides an excellent review[9].

1.2.1 Sputtering

Sputtering is a deposition technique that uses ions from a plasma to strike atoms off a target, which is made of the desired thin film material, that are then deposited on a substrate. A plasma is formed in a vacuum chamber using an inert gas such as argon. A simplified schematic is shown in Fig. 1.3.

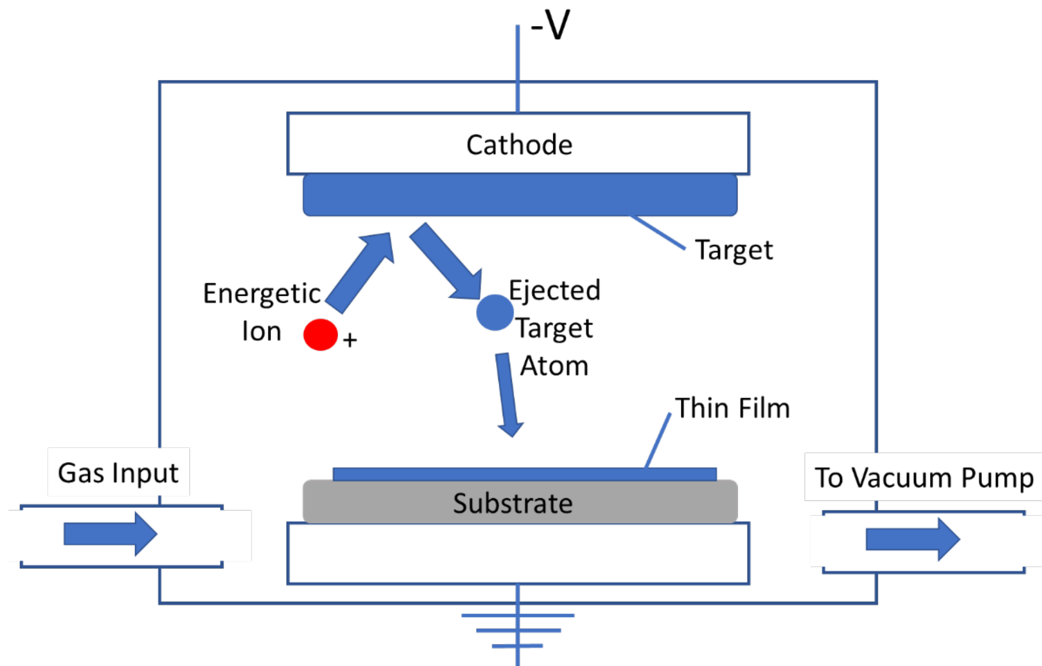

Figure 1.3 Schematic of sputtering process

A chamber is first evacuated using a vacuum pump. A small, controlled amount of gas is inserted into the chamber, typically using a mass flow controller (MFC). The pressure is typically kept between a few millitorr to one hundred millitorr. A negative bias is applied to the target, usually about -1000 V. The gas is ionized, and a plasma is formed. The negative bias on the target causes ions to impact the target and knock off atoms. These atoms then form a uniform thin solid film on a substrate. The substrate can be heated, biased positively or negatively, to change the type of film deposited. This deposition can be done at low temperatures which is advantageous for some situations where the substrate cannot withstand high temperatures. It is also possible to insert a different type of gas that can react with the target, the deposited film, or both, causing a different type of film to form on the substrate. Sputtering experiments for different types of carbon thin films will be discussed more in Chapter 2.

1.2.2 Chemical Vapor Deposition

Chemical vapor deposition is a technique that uses one or more gas precursors to chemically react and form thin solid films on a substrate (Figure 1.4).

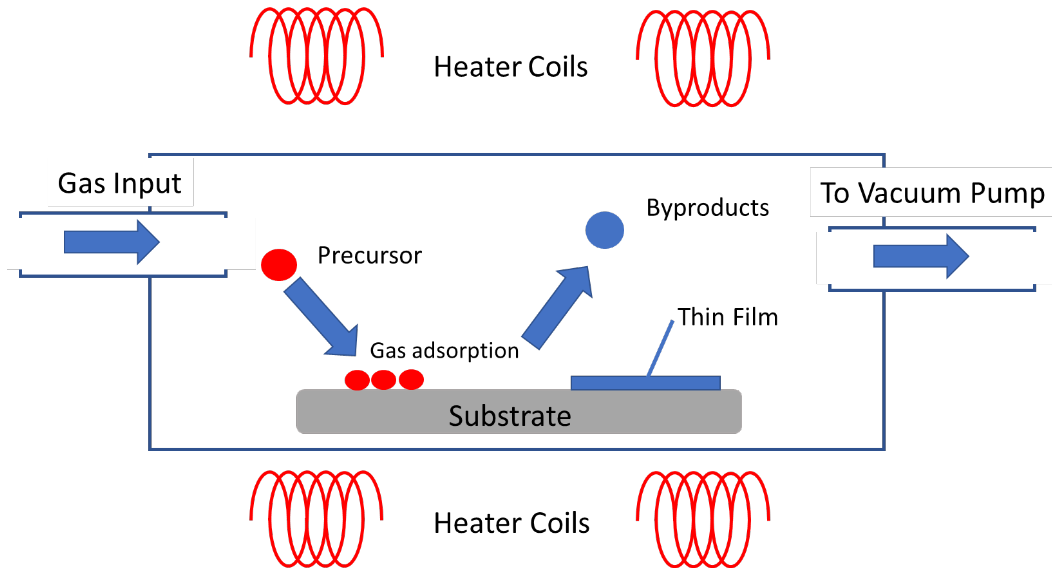

Figure 1.4 Schematic of Chemical Vapor Deposition Process

One or more gases are introduced into a chamber, typically at low pressure but it can be done at standard pressure or higher pressures. A substrate in the chamber is heated, using a variety of techniques like infrared lamps or convection from heated coils. The elevated temperature in the chamber or on the substrate will cause the gas to chemically react, and some products will adsorb on the substrate leaving a desired film on a substrate surface. Unwanted byproducts of the reaction are carried away by the vacuum system. The reaction can consume some of the substrate in creating a new film or leave a film on the substrate surface. This results in a thin solid film with good conformality.

1.2.3 Spin-coating

Spin-coating is a technique that uses a liquid solution applied to a spinning substrate to leave a thin uniform developed film on the substrate surface[10]. A substrate is cleaned to make sure there are no particles on the surface, as these will disrupt the coating process. A substrate is

placed on a chuck which uses a vacuum to hold the substrate and spins the substrate at hundreds or thousands of rotations per minute. A solution is placed on the center of the substrate before spinning, or while the substrate is spinning. The spinning of the substrate will cause the solution to spread uniformly over the substrate surface. The substrate, now coated uniformly in solution, is then heated to cure the solution, leaving a uniform solid film on the surface.

1.2.4 Photolithography and Reactive Ion Etching

Reactive ion etching is a technique to remove unwanted films and is typically used with one or more polymer etch resist layers. The polymer etch resist layers are usually patterned with photolithography to etch a precise pattern in the desired film (Figure 1.5). Photolithography takes advantage of special polymers that interact with light, called photoresist. Photoresist forms or breaks chemical bonds when exposed to ultraviolet light. Spin-coating is used to apply a solution that will leave a uniform film of photoresist on a substrate surface. To form a pattern, a mask is typically constructed using chrome patterned onto glass. The mask is used with an ultraviolet light source to expose specific areas of polymer, which will form a desired pattern. After exposure to ultraviolet light through the mask, the polymer is developed, by immersing it in a liquid that removes weaker polymer layers. Depending on the type of photoresist, exposure to ultraviolet light can weaken the polymer, allowing those areas to be removed during development. Other types of photoresist will form stronger bonds when exposed to ultraviolet light, and this type of photoresist will retain the pattern exposed to ultraviolet light. Once the photoresist has been patterned, the underlying film is ready to be patterned using reactive ion etching. Like sputtering, in reactive ion etching a plasma is formed with a reactive gas in a vacuum chamber. The gas is chosen so there is a suitable chemical reaction with the film that is desired to be etched. A bias is applied to the substrate which drives ions against it. These ions

chemically react with and volatilize the surface film which is then removed by the vacuum system. Ions can also impact the film with enough force to sputter particles off, and physically remove them as well as chemically remove them. While the gas and etching conditions are chosen to primarily remove the desired film, all exposed layers are typically removed to some degree, and the photoresist must be thick enough for the underlying film to be etched while protecting areas that are to remain. The rate at which a desired film is removed compared to a resist or other film is referred to as selectivity. After the etch is completed, the remaining photoresist is removed, or stripped. This is done either using a liquid that can dissolve the photoresist, or using a reactive ion etch that is very selective and will only remove photoresist.

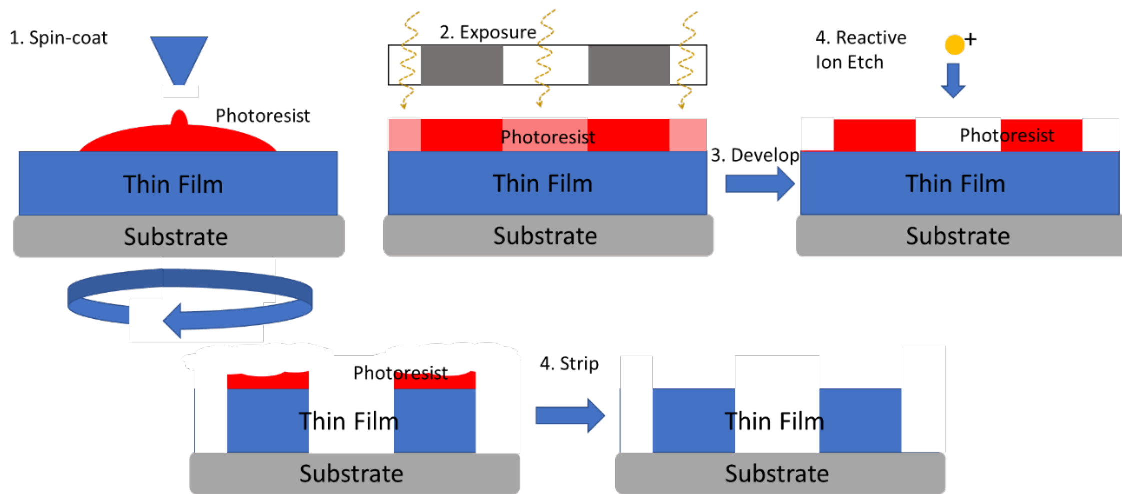

Figure 1.5 Schematic of photolithography and reactive ion etch process

1.3 Characterization Techniques

To understand the different films behavior, techniques common for investigating thin films are used and are briefly reviewed below. These methods are also reviewed by Ohring[9], and some other literature is also referenced for more detailed descriptions.

1.3.1 Atomic Force Microscopy

An atomic force microscopy (AFM) is one of a type of surface characterization tools known as scanning probe microscopes. This tool uses a probe to scan a surface and measure its properties. The basic idea behind this microscope is to create a small, ideally atomistic, tip at the end of a cantilever. As this tip is moved closer to a surface, the deflection of the cantilever provides a measurement of the force between the tip and the surface[11]. The probe is controlled by piezo-electric actuators, some that move the sample or the probe in perpendicular directions and a one actuator that moves the sample and probe closer together. The deflection of the cantilever is measured by shining a laser on the cantilever, which is reflected onto an array of photodiodes. A common method for measuring topography is tapping-mode[12]. A piezoelectric driver vibrates the probe at its resonant frequency. As the probe is moved close to the surface, the amplitude of oscillation will change, and the piezoelectric tube will adjust the height of the probe to keep the amplitude constant. The relative height is recorded as the tip is scanned along the surface, and a map is built of the surface topography.

1.3.2 Stress and Stress Measurement.

When thin films are deposited onto a substrate, oftentimes the deposited atoms or molecules are in an excited state that becomes quenched as a solid film is formed. The resulting film typically does not have ideal interatomic spacing but cannot relax because it is attached to a rigid substrate. Also, even without excitation of incoming atoms, there can be stress in thin films from bonding to a substrate with a dissimilar atomic spacing. First described by Stoney in 1909[13], this technique is now used extensively in the semiconductor industry, as well as the fields of materials science and engineering[14]. The stress in a deposited thin film is calculated using properties of a substrate, the thickness of the film, and the deformation of the substrate.

The stress from the deposited thin film causes the substrate to bend and so the substrate surface is measured before and after thin film deposition. The thickness of the film, substrate and the substrate stiffness and bending are used to compute the film's stress. This is used in Chapter 2 in investigating the material properties of sputtered amorphous carbon.

1.3.3 Scanning Electron Microscope

A scanning electron microscope (SEM) focuses a beam of electrons onto a surface and moves this beam across the surface while measuring the emission of secondary electrons, or other signals, from the surface. A tungsten filament, or other type of electron source such as a LaB_6 crystal, has a voltage applied between itself and a metal grid. The electron source is sometimes also heated to assist in extracting electrons. Electrons are accelerated using an anode to an energy of ~20 keV to obtain good resolution and image contrast. The electrons then pass through a collection of electron lenses that condense and focus the beam so that it has a small spot size on the specimen (< 10 nm). Scan coils are used to scan the beam along the surface of the sample. Using the location of the electron beam and the signal from emitted electrons, an image can be constructed of the surface. Typically, secondary electrons are used, and these can provide a fine image of the surface topography. Under the right circumstances features on the nanometer scale can be resolved[1]. Backscatter electrons are electrons that undergo numerous elastic interactions with the specimen and are scattered back out of the surface. These electrons can add more elemental information to an image, as the rate at which electrons will backscatter is dependent on the atomic number of the atoms on the surface. In addition to electron imaging, SEMs are also typically coupled with EDS detectors for additional analytical capabilities.

1.3.4 Transmission Electron Microscope

A transmission electron microscope (TEM) uses a beam of electrons passing through and interacting with a sample[15]. Because the electrons must pass through the sample, these samples are typically very thin, <100 nm. Similar to an SEM, electrons are emitted from a tungsten or other source and accelerated, although usually to a much higher energy, ~300 keV. The beam of electrons is focused on a sample and pass through it. After electrons pass through the sample, additional electron lenses can magnify the image and depending on what kind of information is desired, the transmission image can be passed directly to a CCD. Images from the main beam are called bright field images. An aperture can also be used to look at electrons that are diffracted at angles away from the main beam and these images are called dark field images. Diffraction patterns can also be imaged, generating crystallographic information. Like a SEM, TEMs are also typically coupled with EDS detectors, allowing chemical information to be obtained in addition to the electron imaging capabilities. Since electrons are passing through samples, it is also possible to obtain the energy lost from electrons in inelastic collisions with electrons in the sample. This is called electron energy loss spectroscopy (EELS)[16]. EELS can give information of the sample through plasmon interaction, elemental information through interaction with core electrons from atoms in the sample, as well as chemical bonding information from interactions with valence electrons in the sample. In Chapter 2, EELS analysis is used to calculate the ratio of different types of carbon bonds in an amorphous carbon sample.

1.3.5 X-Ray Diffraction

In x-ray diffraction (XRD), a beam of x-rays of a specific energy is focused onto a flat surface at a specific angle. As the angle between the incident beam and the surface is changed, a CCD or other device measures the intensity of reflected x-rays. The structure of the surface can

cause the x-rays to reflect more intensely at specific angles, which is used to measure the crystal dimensions of the substrate. The orientation of crystals in the substrate relative to the surface is also measured and in some cases stress and defects can be detected.

1.3.6 Raman Spectroscopy

In Raman spectroscopy, a laser is focused on a surface and the reflected light is filtered to measure only light that has shifted wavelength[17]. The photons that have shifted wavelength have interacted with phonons in the surface and this shift is measured with a spectrometer. Carbon films have good Raman sensitivity with laser wavelengths in the visible spectrum, giving information that can be used to distinguish between amorphous carbon, single layer, bilayer, multilayer graphene and other types of carbon[18, 19].

1.3.7 Bulge Testing

Bulge testing measures the deflection of a thin film as pressure is applied to one side of the film. By measuring the deflection of the film while pressure is applied, the stress and strain of the film can be calculated as pressure is increased and the film is stressed to failure. This will be described more fully in Chapter 3.

1.4 Scope of Work

EDS is a powerful technique able to quantify chemical composition for most materials, and in a TEM this analysis can have spatial resolution in the tens of nanometers. In an SEM, surfaces can be quickly analyzed quantitatively and with enough speed that surfaces can be mapped for composition. Elements with low atomic weight are more difficult to quantify because they emit lower energy x-rays. X-ray detector windows with improved x-ray transmission are needed to gain better performance for measuring these elements that are important in materials

science. Because of carbon's low atomic number, amorphous carbons chemical resistance, and its specific strength in some forms, it is a promising material for x-ray detector windows.

In Chapter 2 a study of sputtered amorphous carbon is detailed. Sputtered amorphous carbon was used to protect a metal film that made part of an x-ray window. This carbon film along with similar carbon films sputtered under different conditions were investigated. This work was published in JVST A[20]:

J. Rowley, L. Pei, R. C. Davis, R. R. Vanfleet, S. Liddiard, M. Harker and J. Abbott, Journal of Vacuum Science & Technology A: Vacuum, Surfaces, and Films **34** (5) (2016).

Bulge testing is a critical technique for measuring the tensile strength, deflection, as well as burst pressure of a thin film. Chapter 3 details the construction a bulge tester device, that is being submitted to the Journal of Scientific Instruments:

J. Rowley, K. Larsen, J. Abbott, R. R. Vanfleet, and R. C. Davis. *Automated Burst Tester of Large Diameter Samples over a Large Pressure Range With Displacement Measurement.*

Bulge testing was used to examine several models of x-ray windows, along with silicon nitride membranes. This work was summarized in a poster for the Microscopy and Microanalysis conference in 2015. Chapter 3 also contains some results from proceedings that were published for this conference[21]:

J. Rowley, K. Berry, R. Davis, R. R. Vanfleet, S. Cornaby, M. Harker and R. Creighton, Microscopy and Microanalysis **21** (S3), 2005-2006 (2015).

Chapter 4 discusses a study of many-layer graphene films, investigating x-ray transmission, thickness uniformity, and burst pressure. This work has been submitted for publication.

J. Rowley, S. Lehnardt, K. Larsen, J. Abbott, R. Vanfleet, R. C. Davis. *Uniformity of Suspended Many-layer Graphene Membranes: Impact of Nickel Foil Thickness and Surface Microtexturing*

Further work is needed to generate many-layer graphene that will withstand the pressure needed for an x-ray detector window. In chapter 5, potential improvements in film growth are discussed and some initial work done to grow these films at BYU is described.

Chapter 2 Sputtered Carbon as a Corrosion Barrier for X-Ray Detector Windows

2.1 Introduction

Amorphous carbon thin films deposited by plasma enhanced chemical vapor deposition (PECVD) and magnetron sputtering are widely used as gas barriers[22-33]. Sputtered amorphous carbon thin films have also been shown to be effective corrosion resistant coatings[34-37]. The x-ray transmission for low energy x-rays is strongly material dependent, with a general trend of higher transmission with lower atomic number. Carbon thin films are attractive materials for x-ray detector windows because carbon's low atomic number (low Z) can allow high x-ray transmission in the low energy regime (~50-1000 eV, see Figure 2.1) of energy dispersive x-ray spectroscopy (EDS), where x-rays are used for elemental analysis. Sputtering is a low temperature physical vapor deposition (PVD) process that is easily integrated with other PVD steps.

Much prior research on amorphous carbon thin films has focused on achieving high hardness[38], scratch resistance, and low friction[39], producing films with a large percentage of sp^3 carbon-carbon bonds. Unfortunately, high sp^3/sp^2 ratios in sputtered carbon thin films are associated with high compressive stress[40, 41]. A subplantation model applied by Davis[42] and Robertson[43] successfully predicts the relationship between high sp^3/sp^2 ratios and high levels of compressive stress occurring together at higher particle deposition energies.

High intrinsic stresses can result in delamination, and if the surface being coated is fragile, as in a thin suspended membrane, large intrinsic stress can rupture the membrane. Sputtering can result in low stress carbon films and these films can be advantageous in applications where high sp^3 content and correspondingly high hardness are not needed.

Experimental results show low compressive stresses at low ion bombardment energies, this is consistent with subplantation model predictions. Jensen and Hoffman used pressure to effectively control the stress in sputtered carbon thin films, where the magnitude of the intrinsic stress passed through a minimum as the films transitioned from being in compressive stress to tensile stress[44]. Others have successfully deposited thin carbon films with low stress by sputtering using combinations of high pressures[45] , introducing and increasing hydrogen flow rates during deposition[46], substrate heating[47] and biasing substrates[41].

Here we explore high sp^2 content DC magnetron sputtered carbon for incorporation into x-ray windows as a corrosion resistant coating. In fact, due to its excellent x-ray transmission (see Figure 2.1), carbon (deposited using high temperature chemical vapor deposition) has previously been used as a window material for low energy x-rays[48-50].

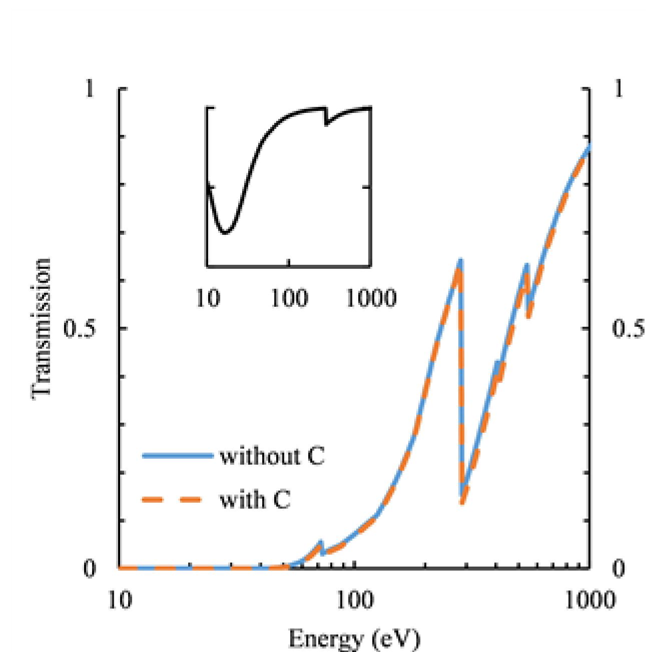

Figure 2.1 (Color online) Comparison of a polymer supported aluminum thin film used in an x-ray detector window with and without a carbon corrosion barrier. The largest loss in transmission is only 2.2% at ~350 eV. Inset is the x-ray transmission of a 10 nm thick carbon film. Transmission values were calculated using the CXRO x-ray database (Lawrence Berkeley National Laboratory).

In this prior use carbon was the sole structural element of the window which required that it:

1. function as a gas barrier,

2. have sufficient strength to withstand 1 atm of pressure, and

3. allow for high transmission of low energy x-rays

Our corrosion resistant carbon thin film has quite different requirements. Here we want a film that:

1. is deposited at low temperature (< 100 C) and thus is compatible with a wide range of x-ray window fabrication process,

2. provides high corrosion resistance when deposited on thin aluminum films,

3. has a high ultimate strain with low intrinsic stress,

4. has high transmission for low energy x-rays.

In contrast to Huebner et. al, who needed high strength, our needs were for high strain before failure. Also, prior sputtered-carbon literature has focused on obtaining high hardness films and researchers have primarily used nanoindentation to obtain the mechanical properties of stiffness and hardness. Because of our requirements for high strain and low stress, we chose bulge testing[51, 52] and wafer curvature measurements to determine modulus, tensile strength, and intrinsic stress. These measurements now allow us to predict mechanical performance under tensile load enabling integration of this material into a functioning x-ray window. We have found no prior literature that provides bulge testing data on sputtered carbon.

We have also characterized the sp^3/sp^2 content of our films using EELS[53], which avoids some of the interpretation problems inherent in spectroscopic ellipsometry[54] analysis and Raman

analysis[55] of sp^3/sp^2 content. We used Raman analysis for qualitative measurement of hydrogen content[19] and we quantitatively measured hydrogen content in a reactively sputtered film using carbon hydrogen nitrogen (CHN) elemental analysis.

We sputtered carbon films at various thicknesses with argon, mixtures of argon and ethylene and mixtures of argon and methane for testing. Eight nm thick carbon films were deposited on NaCl shards and floated onto TEM grids for EELS. EELS showed less than 5% sp^3 content. Stress was measured on 170 nm thick carbon films that were sputtered with no reactive gas yielding a stress of 0.085 GPa. Stress was measured on films sputtered with reactive gases yielding stresses from 0.45 GPa down to 0.21 GPa. The lowest stress in the reactive sputtered films was a 100 nm film sputtered in 10% ethylene flow in argon.

A 1 micron thick reactively sputtered (10% ethylene flow in argon) film was deposited on a release layer for bulge testing and CHN analysis. The CHN analysis showed 55 at.% carbon, 39 at.% hydrogen, and 5 at.% oxygen. The carbon films strain at failure was ~3%, as determined by bulge testing. This is a much higher strain than the limiting strain of the aluminum thin film (0.02%[56]) the sputtered carbon will coat, and also is much higher than an alternative carbon coating of CVD diamond like carbon (0.004%[57]). Very thin carbon films (~10 nm) were deposited on a polymer-supported evaporated aluminum film, exposed to humidity, and analyzed by optical microscopy. There was no observable corrosion on the carbon protected film, while aluminum films without the carbon coating showed significant corrosion.

2.2 Experimental

2.2.1 Hydrogenated Amorphous Carbon Reactive Sputtering

The DC magnetron method was employed using ethylene in argon, methane in argon, or only argon in a Lesker PVD 75 using a 3” 99.999% pure graphite target and 56.6 W/cm^2 (400 W). The pressure was kept at 7 mtorr, with gas flow rates ranging from 79.4 to 83.4 sccm, where reactive gas comprised 0%, 4%, 9%, and 17% of the total flow. Deposition rates were between 1-3 angstroms/second, and monitored by quartz crystal microbalance, with a target to substrate distance of 20 cm. Films were deposited onto the following substrates: silicon wafers for stress measurements, NaCl shards for TEM analysis, polyvinyl alcohol (PVA) coated silicon wafers for CHN analysis, aluminum coated silicon wafers for Raman spectroscopy, and polymer aluminum stacks for corrosion testing.

2.2.2 Corrosion Resistance Testing

For large area characterization of corrosion, films were prepared for optical transmission microscopy. Thin (<50 nm) films of Al were evaporated onto supported polymer membranes. Sputtered amorphous carbon coated one sample, and one sample was left bare. The samples were fixed in stainless steel mounts and the backsides of both samples were protected with Parafilm® to prevent diffusion of water through the polymer to the backside of the aluminum. The samples were then placed in an environmental chamber at Moxtek, Inc., and exposed to 80% relative humidity at 40° C for 10 hours. Results were evaluated by optical microscopy.

2.2.3 Intrinsic Stress Measurement

Stress was measured by obtaining the curvature of wafers using a Zygo white-light interferometer before and after carbon deposition. A Stoney’s equation[38] approach was used to extract intrinsic stress and the results are shown in table 2.1. Silicon wafers with a saddle type

profile were found to increase the uncertainty in this measurement, so care was taken to use wafers with a dome type profile.

2.2.4 EELS

Carbon was sputtered onto NaCl shards with and without reactive gas. After sputtering, the films were floated off in de-ionized water and picked up onto copper TEM grids. EELS was performed on a Tecnai F20 TEM. The energy resolution during these scans ranged from 0.9-0.6 eV. The data's π^* peaks were aligned at 285 eV for comparison.

The sp^3/sp^2 ratios were determined by taking ratios of integrated peak intensities and comparing these ratios to those of a reference. The amorphous carbon support film on a TEM grid was used as the 100% sp^2 reference in this work.

2.2.5 Raman Spectroscopy

A Renishaw® Raman Spectroscopy system at Utah Valley University, Orem, UT, was used. Carbon was sputtered onto silicon wafers with a layer of sputtered aluminum. The aluminum layer was used to enhance reflectivity. A 10x objective was used with a 532 nm excitation laser. Data was acquired for 1 minute, 3 different times, and then summed together to produce each spectrum.

2.2.6 Bulge Testing for Determination of Modulus and Strength

Carbon thin films were sputtered onto silicon wafers that had previously been dip-coated with Daecoat 550 from Daetec. Metal washers were then glued to the surface, the carbon was scored around every washer, and then the entire wafer was put into deionized water to dissolve the Daecoat 550 and release the film.

The washers with suspended films were then attached to a pressurized air apparatus and placed under an optical microscope, with a 10x objective. As pressure was increased, a film's

bulge height was analyzed by measuring the vertical movement needed to bring the film into focus. The pressure vs. displacement data allows for the extraction of mechanical properties of the film using a previously demonstrated model[39]. The uncertainty in this height measurement was estimated at ± 2 microns.

2.2.7 CHN Elemental Analysis

In order to perform a CHN microanalysis, the sputtered carbon had to be released from the wafer and collected. This was accomplished by sputtering onto silicon wafers with a PVA release layer. The wafer was then placed in deionized water to release the film. The carbon material was collected by filtering. Subsequent rinsing and filtering were done 6 times to eliminate any PVA contamination. About 50 mg of carbon flakes were collected and sent for CHN and oxygen testing by Midwest Microlabs.

2.3 Results

Corrosion testing results are shown in Figure 2.2 for a set of evaporated Al thin films with and without a carbon coating. The amorphous carbon coating has retained the uniform state of the Al, while the film without a coating underwent significant corrosion when both were exposed to 80% relative humidity at 40° C. These optical transmission images reveal that the carbon coating is effective in limiting corrosion.

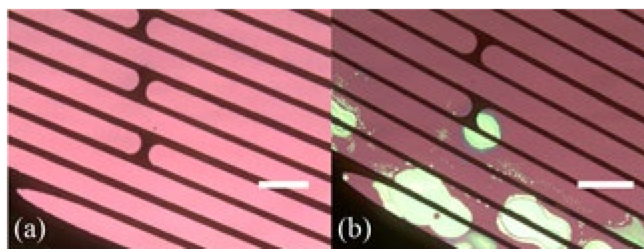

Figure 2.2 (Color online) Transmission optical micrographs of an aluminum thin film deposited on a polymer membrane and subjected to corrosion testing. The dark lines are a support structure holding the polymer membrane. The aluminum film shown in (a) has a carbon coating, while the film shown in (b) does not. Scale bars are 0.5 mm. The non-uniformity in transmission in the uncoated sample (b) indicates corrosion.

The films' intrinsic stress measurements are shown in table 2.1 row 2. All samples demonstrated a stress below 0.5 GPa (compressive). Varying the type of gas used for reactive sputtering, and even sputtering with no reactive gas, did not produce high levels of stress.

Table 2.1 Thickness, stress and sp^3/sp^2 ratio data for sputtered carbon films. Reactive gases shown in the column headings are diluted in argon. Asterisks are used to indicate samples with significant hydrogen content.

	No Reactive gas	4% Ethylene*	10% Ethylene*	4% Methane*	10% Methane*
Thickness(nm)	166/169	105	95	243	263
Compressive Stress (GPa)	0.0758/0.0922	0.393	0.214	0.455	0.31
sp^3/sp^2 ratio	2±5%	4±5%	1±5%	2±5%	6±5%

The sp^3/sp^2 ratio was investigated using EELS[53]. Two sets of EELS spectra, one with 10% ethylene in argon sputtered sample, and the other sputtered with only argon, are shown in Figure 2.3. The background has been stripped from these spectra and the π* peaks have been aligned at 285 eV. In each set, the sp^2 reference and a high sp^3 content spectrum are included for comparison. Only sp^2 bonding contributes to the π* peak while both types of bonding contribute to the higher energy peaks. Thus, analysis was done by taking the ratio of the intensity of the π*

peak ($I_{\pi*}$: from 281-287.5 eV dashed line orange box) to a large window including both the π* and σ* peaks (I_{total}: 281-310 eV dotted blue line box, I_{total}). This ratio is normalized by the ratio similarly obtained, from the reference carbon. The result is the sp^2/sp^3 ratio of the sample which is easily converted to the sp^3/sp^2 ratio.

$$\frac{\left(\frac{I_{\pi*}}{I_{total}}\right)_{sample}}{\left(\frac{I_{\pi*}}{I_{total}}\right)_{reference}} = \frac{sp^2}{sp^3} \quad (2.1)$$

$$\left({sp^3}/{sp^2} \right) = 1 - \left({sp^2}/{sp^3} \right) \quad (2.2)$$

The sp^3/sp^2 results for 5 different samples can be seen in table 2.1 row 3. No samples had significant sp^3 content.

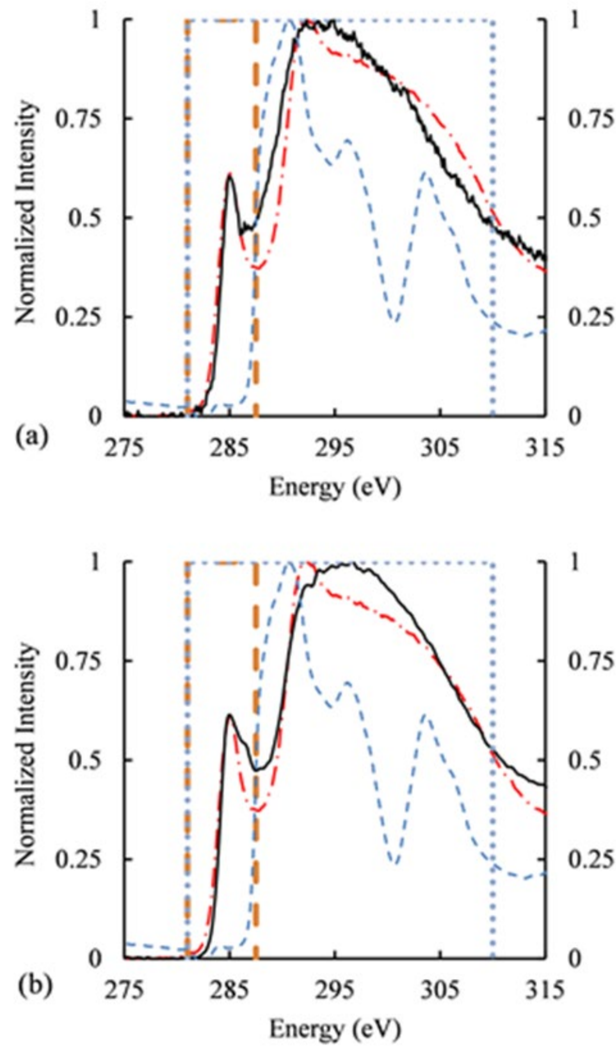

Figure 2.3 (Color online) EELS characterization of chemical bonding for a reactively (10% ethylene flow) sputtered film (a), and a sputtered carbon thin film (b). The background was stripped out and energy was normalized to the maximum value in this range. The smaller box (dashed line) is the area used to calculate $I_{\pi*}$ while the larger box (dotted line) is the area used to calculate I_{total}. The sp^2 reference is the red dash dot line and nano-diamond is the blue dashed line. The nano-diamond curve has little to no signal in the π area, demonstrating the lack of sp^2 bonds. The data from sputtered samples (solid black lines), are very similar to the sp^2 reference, indicating the large percentage of sp^2 bonding.*

TEM diffraction patterns showed only diffuse scattering demonstrating the amorphous nature of the carbon thin films.

Raman spectroscopy demonstrated differences in hydrogen content. Three samples were prepared for Raman spectroscopy: one with no reactive gas, one with a 10% gas ratio of ethylene, and one with a 10% gas ratio of methane. A sloping background is indicative of hydrogen content[41], thus the presence of different background slopes of these spectra (shown in Figure 2.4) indicate there are differences in hydrogen content.

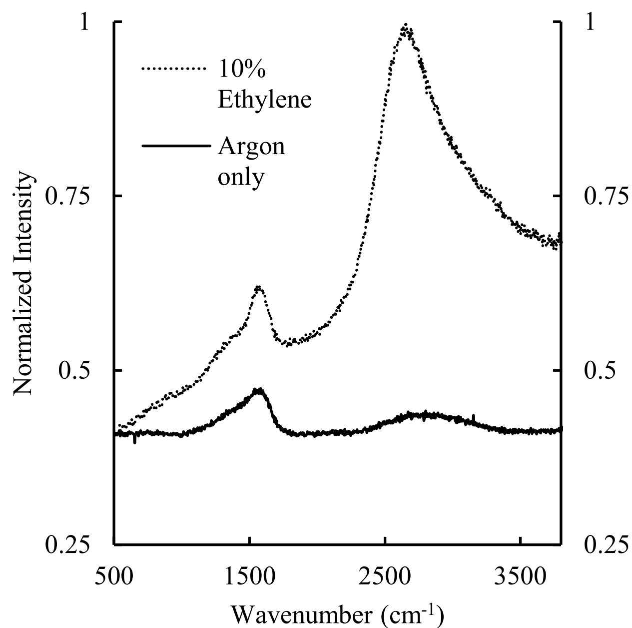

Figure 2.4 Normalized Raman spectra of carbon sputtered with (10% ethylene in argon) and without (argon only) reactive gas. The background slope of the reactively sputtered sample in the wavenumber range depicted indicates hydrogen content. The background in the argon only sputtered film is essentially flat in this range, consistent with no hydrogen content.

CHN and oxygen elemental analysis was done to quantify hydrogen and oxygen content. Amorphous carbon was reactively sputtered with a 10% gas flow of ethylene, as stated previously, onto a silicon wafer that had been dip-coated in Daetec 550. After sputtering, the film was released in deionized water. The sputtered carbon was transferred to successive baths of deionized water, prior to removal from the water using a Teflon filter. In this way, 50 mg of sputtered amorphous carbon was collected into a glass vial and sent for analysis. Tests showed

the oxygen wt.% from 10.49-10.68, and the hydrogen wt.% from 4.85-5.06. The balance of mass was carbon with a nitrogen content less than 0.9%.

An example of data obtained is shown in Figure 2.5, which was used to determine the Young's moduli of the membranes (2-5 GPa) and ultimate strengths (50-150 MPa). These are the first moduli and tensile strength measurements that have been reported for sp^2 sputtered carbon thin films.

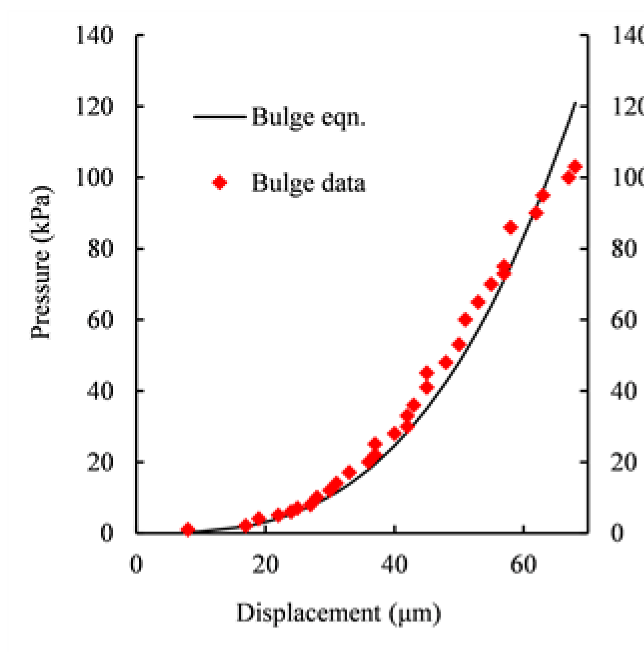

Figure 2.5 Pressure vs. displacement for an amorphous carbon suspended film (1.1 mm diameter circle, 1 μm thick). The bulge test equation is a good fit until the breaking point at around 100 kPa. The analysis using the bulge equation gives a modulus of 5 GPa and a strength of 150 MPa.

2.4 Discussion

The integration of this sputtered amorphous carbon into a functioning mechanical device necessitated not only the quantitative analysis of film structure and content, but also knowing its performance under tensile load. The mechanical properties measured by bulge testing show that the reactively sputtered (10% ethylene flow in argon) amorphous carbon can withstand a high

strain (~3%). This is well beyond the needs of our application, this significantly exceeds the limiting strain of the aluminum film (0.2%[56]) it will be used to protect.

Low stress was seen in our films which were deposited at high pressure with and without reactive gases. The lowest stresses seen were in films deposited without reactive gases (0.08 GPa); these are comparable to the lowest stresses reported in the literature. The films were composed entirely of sp^2 carbon which is consistent with predictions of low sp^3 content and low stress being achieved at high pressures[58]. Reactively sputtered films also showed low stress. The behavior of stress vs. hydrogen gas concentration (i.e. increasing initially and then gradually decreasing) is consistent with the findings of Rubin et al[46]. The lowest stress in reactively sputtered films that we observed (0.21 GPa) was at conditions of 10% ethylene flow in argon. This low stress is well below the stress where delamination in sputtered carbon films has been seen (> 4 GPa[41]).

In summary, reactively sputtered sp^2 carbon films can be used as corrosion resistant coatings in x-ray windows. They are capable of high strains, showed low stress, and very thin coatings of these films effectively protected aluminum films from corrosion.

Chapter 3 Automated Burst Tester of Large Diameter Samples over a Large Pressure Range With Displacement Measurement

3.1 Introduction

Measuring the mechanical properties of thin films requires different techniques than those used for characterizing bulk materials. Bulk materials are commonly mechanically characterized by pull testing. Thin film samples are difficult to prepare for pull testing, requiring extensive microfabrication, as well as specialized equipment[59]. Also, effects of stress concentration, intrinsic stress, and complications from the edges of the sample have a more pronounced effect in thin films. Bulge testing removes some of these difficulties[60] in testing thin films. To bulge test a material, a thin film is suspended on a circular or rectangular support frame, while a gas pressure is applied on one side of the film and the film displacement is measured. More recently, bulge testing was extended from elastic deformations to plastic deformations of thin copper films[61, 62]. This work describes a reconfigurable bulge tester using commercially available scanning optical sensors to bulge and burst test simple, and complex membranes.

3.2 Bulge Tester Design

The bulge tester that we designed and built had four main parts:

- A laser displacement sensor, Keyence LK-G5001 controller with a LK-H052 sensor head, used to measure the out-of-plane displacement of the suspended film.
- Opto-mechanical hardware and a stepper motor (Newport NSA12 with NSC200 controller) used to control the lateral position and scanning of the displacement sensor along the thin-film.

- A pressure regulator, Proportion Air QPV2, used to control the gas being applied to the thin film, along with feedback and pressure measurement from a pressure transducer, Omega PX-219.
- An Aera FC-7810 mass flow controller (MFC). The MFC was in a fully open state and was used to measure the flow of gas through the device. This allowed the device to detect small leaks in the setup or cracks in the film, with a small measurable flow, as well as catastrophic film failure, when the flow jumped to a relatively high rate.

Signal collection and control of the apparatus was done using a custom National Instrument LabVIEW program. Signal acquisition included digital communication over USB with the Keyence LK-G5000, position signal and control with the NSC200 over an RS-485 interface, and analog signals acquisition and control for the pressure regulator, MFC and pressure transducer using a National Instruments PCI-6041E DAQ. Computer control of the system as well as data recording was done within LabVIEW.

To bulge test a sample film, samples were glued or placed between two metal fixtures, pieces of stainless steel with square or rectangular holes, or metal washers. If the film was already attached on one side to a rigid support, for example a thin film suspended on a piece of silicon, a washer would be glued to the top for bulge testing. The metal fixtures, with the sample membrane between them, would be placed on top of a gasket on an aluminum block. The aluminum block had ports that allowed gas pressure to be applied to the bottom of the membrane through a cylindrical passage through the side of the block (see Figure 3.1).

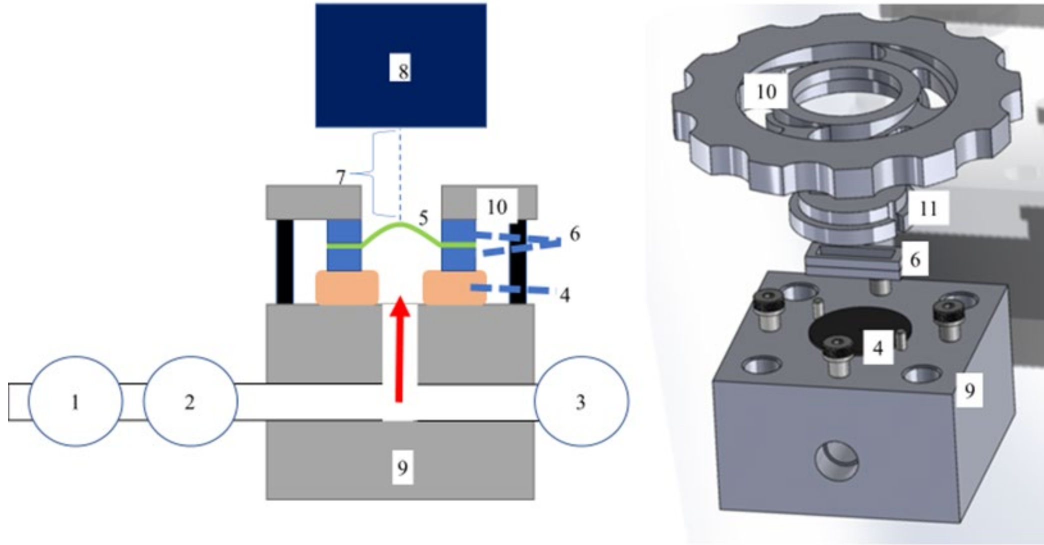

Figure 3.1 Cross section and 3D render of bulge test device. Pressure was controlled and measured through a pressure regulator (1) and pressure transducer (2). A mass flow controller (3) was kept fully open and measured airflow to quantify when the membrane broke vs when there was slight leaking from the setup or small cracks in the membrane. A sample membrane (5) was attached to or placed between two metal fixtures (6). The film with fixtures was placed on a gasket (4) and a top clamping piece (10) was screwed down to clamp the film with fixtures in place. A center piece (11) was used to hold the metal fixtures and membrane in place while the top clamping piece was screwed down. After the film was secured, the sensor head (8) was adjusted to scan over the central part of the film, measuring the displacement (7) across the film as pressure was incrementally increased.

A plastic center piece was 3D printed to hold the metal fixtures in place while a top clamping piece would be screwed down over the top, clamping the fixtures to the film and against the gasket, making a pressure tight seal.

3.3 Bulge Testing a Simple Membrane: Silicon Nitride

Silicon Nitride membranes were made with chemical vapor deposition on silicon wafers. The backside of the silicon wafer was etched away, leaving a circular free-standing silicon nitride membrane, with a diameter of 7mm. The membranes were mounted on a metal frame and to obtain a good displacement measurement a colloidal silver solution was airbrushed on the membranes. The small metallic particles allowed the sensor to detect the surface, without having to apply a coating that would change the mechanical properties of the silicon nitride membranes.

Pressure was incrementally increased against the silicon nitride membrane, and at each increment the displacement sensor would be scanned across the surface. The film would bulge with a circular profile, and the height and horizontal position values were fitted using the "Hyper" circle fitting algorithm from Al-Sharadqah and Chernov[63]. Using the pressure measured during that scan step, as well as the radius of curvature, the stress and strain at each pressure step was calculated using equations 3.1 and 3.2[52], which are the equations of stress and strain for a spherical cap. In equations 3.1 and 3.2, R is the radius of curvature of the suspended membrane, t is the thickness, p is the pressure applied to the film and a is the radius of the open area.

$$\sigma = \frac{pR}{2t} \tag{3.1}$$

$$\varepsilon = \frac{\arcsin({}^{a}/_{R}) - {}^{a}/_{R}}{{}^{a}/_{R}} \tag{3.2}$$

The silicon nitride membrane was 500 nm thick and was much smaller than the spanned radius of 3.5 mm, allowing for the assumption that bending stiffness was negligible. Figure 3.2a shows the scanned profiles of the film as pressure was increased from 0 PSI to 20 PSI, in increments of 2.5 PSI. In Figure 3.2b, the stress vs strain was used to calculate the biaxial modulus Y, of 332 GPa. Assuming a Poisson's ratio $\nu = 0.22$, the Young's modulus E, can be calculated using $E = Y(1-\nu)$, yielding a value of 256 GPa. This value was in good agreement with the Young's modulus for CVD thin film silicon nitride reported in the literature[64]. The first two points in the stress vs strain plot were not on the same line as the other points. This is due to the initial strain in the membrane and these points were not well modeled by the assumptions in the bulge equation.

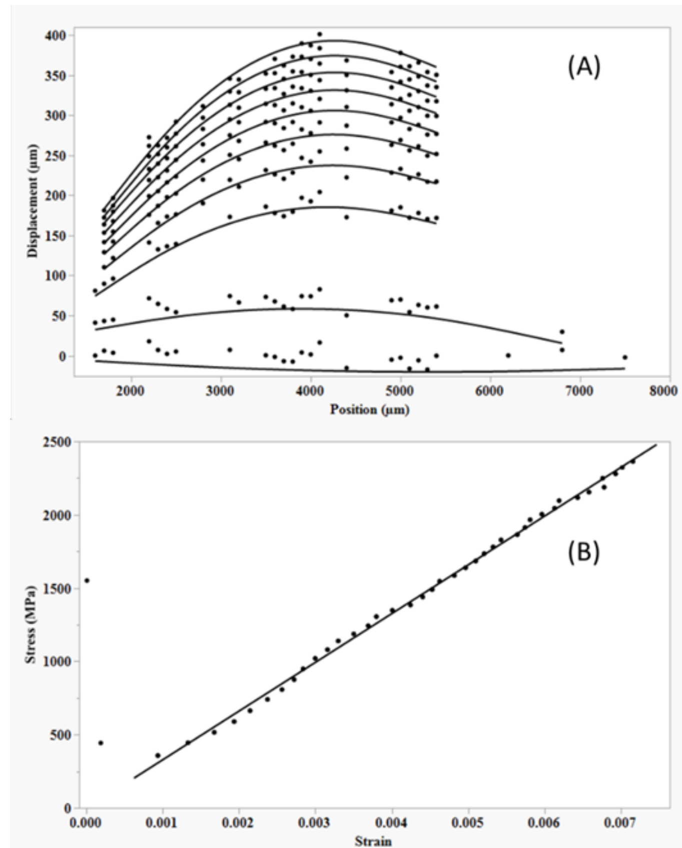

Figure 3.2 Displacement profiles(A) of a 500 nm thick silicon nitride membrane suspended over a circular hole of diameter 7 mm. The displacement profiles in (A) were collected as pressure was increased from 0 to 20 PSI, and the profiles here are in steps of 2.5 PSI. There are some points missing from the right side of the membrane, as pressure was increased these points no longer were reflected in the direction of the sensor, but there are enough points to fit a circular bulge. In (B), a straight line can be fitted well to all but the first two points, and this was used to calculate a Young's modulus of 256 GPa. The first two points are when the film had an initial strain and were not well modelled by the bulge equation.

3.4 Bulge Testing Wrinkled, Relatively Thick Membranes: Aluminum and Copper Foils

Aluminum and copper foils were obtained from Alfa Aesar, 25 µm thick with a purity >99.5%. To prepare the foils for bulge testing foils were first cut into strips, then pressed in between two glass slides to flatten them. After this, they were sandwiched between two stainless steel fixtures. The fixtures had a 4.0 mm by 23.9 mm rectangular hole that was made by wire-cut electrical discharge machining. After machining, the faces and edges were sanded smooth to remove any sharp points. To make sure the setup was leak tight, a small bead of vacuum grease

was applied to the fixtures where they would contact the metal foils. Pressure against the film was increased incrementally up to ~100 PSI, or until the foils broke. At each step, the Keyence displacement sensor scanned along the surface of the foil, capturing the radius of curvature of the bulged foil.

In Figure 3.3a, a series of scanned profiles are shown for an aluminum foil sample that was bulge tested in steps of 2 PSI from 0-52 PSI, when the foil burst. Figure 3.3b shows the stress vs strain, calculated using equations 3.2 and 3.3, for copper and aluminum foil samples. Equation 3.3 describes the stress in a cylindrical bulge, where p is the pressure applied, R is the radius of curvature, and t is the thickness of the membrane.

$$\sigma = \frac{pR}{t} \tag{3.3}$$

The yield strength of the copper and aluminum foils were derived from these plots, and for the aluminum foils which burst, the tensile strength. The initial linear portions of the stress vs strain curves were used to estimate the biaxial modulus, M. The biaxial modulus was used to calculate the Young's modulus using the relation $E = M(1-\nu^2)$, where ν is the Poisson's ratio of the material. Table 3.1 shows these results.

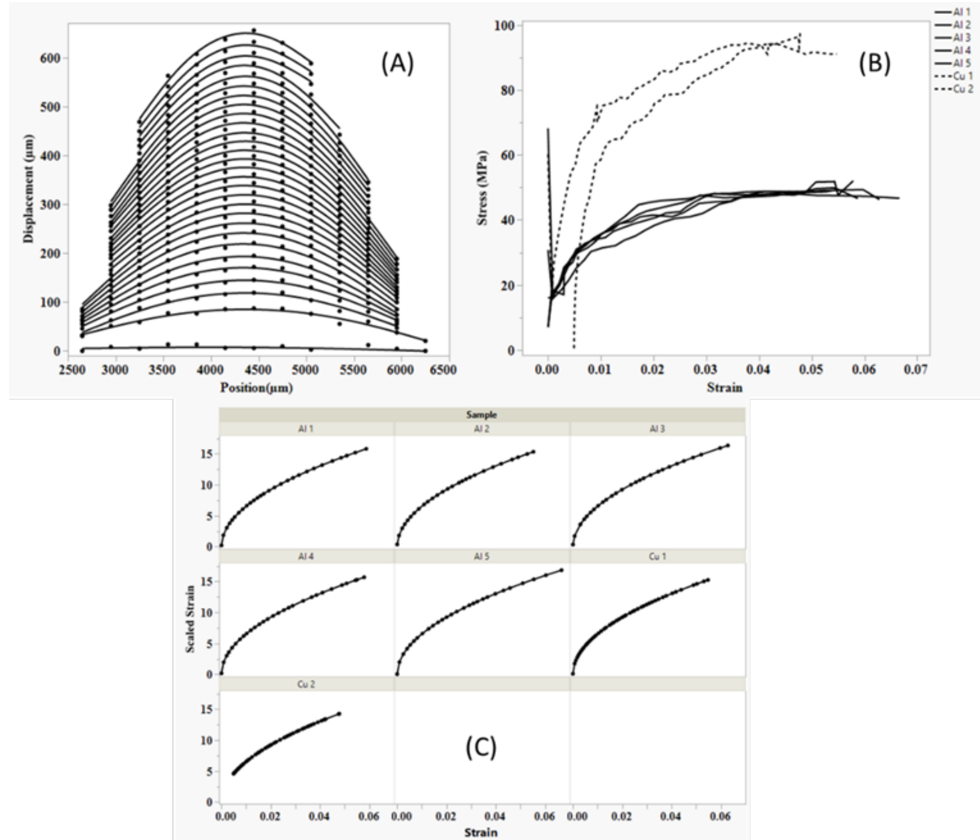

Figure 3.3 (A) Height profiles of a 25µm thick aluminum foil sample suspended over a 4 by 24 mm rectangular hole. Pressure was increased in steps of 2 PSI, from 0 to 54 PSI, at which point the foil burst. (B) are the stress vs strain plots of 25 µm thick aluminum and copper foils that were bulge tested over a 4 by 24 mm rectangular hole. The points at low strain were not well modeled by the bulge equation, and the plane-strain modulus is too low. The stresses at which the aluminum and copper foils began to stretch, as well as when the aluminum foils burst, are reasonably well matched to previous results. (C) shows the scaled strain vs strain for these foils. The scaled strain is < 10 for low values of the strain, meaning that the systematic error strain calculation using the bulge test assumptions is high.

Table 3.1 Calculated mechanical properties of 25µm thick aluminum (Al) and copper (Cu) metal foils from bulge testing the foils over a 4 by 24 mm rectangular hole.

Sample	Plane Strain Modulus (GPa)	Poisson's Ratio	Young's Modulus (GPa)	Burst Pressure (PSI)	Approximate Yield Strength (MPa)	Ultimate Tensile Strength (MPa)
Al1	3.2	0.33	2.85	54	33	50
Al2	3.37	0.33	3.00	54	35	50
Al3	2.83	0.33	2.52	56	35	50
Al4	2.73	0.33	2.43	58	33	52
Al5	2.05	0.33	1.83	54	31	48
Cu1	8.52	0.35	7.48	-	55	-
Cu2	11.82	0.35	10.37	-	50	-

Yield strengths and tensile strengths were reasonably matched to other results of mechanical testing of aluminum foils[65], but the Young's modulus is much lower than the expected value of 70 GPa. The copper foils have similar yield strengths to other results[66], but also have a much lower value than the expected 90-105 GPa. Neggers et al[67] discussed under what situations systemic error can be severe in using the bulge test model. They defined "scaled strain", shown in equation 3.4, where a is the radius of opening, t is the thickness of the membrane or foil and epsilon is the strain calculated using the bulge test equation.

$$\varepsilon^* = \frac{a}{t}\sqrt{\frac{2}{3}\varepsilon} \tag{3.4}$$

In the work of Neggers et al, the scaled strain was used calculate the relative systematic error in the stress and strain obtained from using the bulge test equations. This error is maximized for the strain at low strain values, and when the membrane or foil is relatively thick compared to the radius of opening. From Figure 3.3c, for strain values < 0.01, that were used to calculate the Young's modulus, the scaled strain does not approach values > 13, where the error in the strain is minimized. Also, for the first few measurements of strain for many of the foils, the scaled strain is < 2, where error in the strain measurement is maximized. Also, although the foils were pressed between glass slides to flatten them, there were still wrinkles left in the foils. This interfered with the assumptions used for the bulge test equations. Therefore, it is reasonable to conclude that the low Young's modulus values were caused by these factors: the wrinkling of the foils, and the systematic error in using the bulge equation to model the strain in these foils for this geometry at low strains.

3.5 Conclusion

A bulge tester was assembled from mostly off the shelf parts, capable of measuring both simple membranes, as well as getting useful information out of thicker membranes or foils. A silicon nitride membrane was measured, and the Young's modulus calculated showed good agreement with previous results. Metal foils 25 μm thick were also measured, and the stresses calculated agreed with other results. However, the calculated Young's modulus values obtained from these foils was very low, and was caused by wrinkled state, as well as their relatively thick dimensions making the bulge equations inaccurate for low strains.

Chapter 4 Uniformity of Suspended Many-layer Graphene Membranes: Impact of Nickel Foil Thickness and Surface Microtexturing

4.1 Introduction

Graphene is a remarkable material both for its electromagnetic[68] and mechanical properties[69, 70]. Graphene has a high intrinsic mobility (~5000 $Wm^{-1}K^{-1}$) and high Young's modulus (~1.0 TPa) with an equibiaxial breaking strength of ~100 GPa. One application of the high mechanical strength of graphene is thin film membranes. Single layer graphene is impervious to gases[71], and because of carbon's low atomic number, it has a relatively low attenuation of x-rays. Single-layer graphene routinely spans diameters on the order of 1-5 μm[69], and some have been able to span diameters as large as 10 μm[72]. Graphene films with more than one layer are categorized as multilayer (3-10 layers of graphene) and many-layer graphene films (> than 10 layers of graphene). Many-layer graphene (MLG) films (films with greater than 10 layers of graphene) have been able to span diameters of 7 mm[73].

Chemical vapor deposition (CVD) of graphene is typically done using a catalyst metal foil and vacuum furnace. A hydrocarbon gas is introduced at low pressure and high temperature and breaks down on the surface of the metal, allowing some carbon to dissolve into the metal and form graphene layers on the surface of the metal. CVD growth of graphene using nickel foil substrates can result in multilayer graphene films(3-10 layers of graphene), but achieving uniformity in these films is a challenge[74], with thicknesses varying by a factor of 5 within a film.

Uniformity for single layer graphene on Ni has been achieved by using low pressure and high temperature[75]. Alloying nickel with gold is another method used to improve the uniformity in CVD graphene growth on nickel[76]. In addition, combining alloying the nickel with gold and

using a solid carbon source and a diffusion barrier[77] allowed for extremely large area, uniform, monolayer graphene to be formed. Using single crystal nickel, researchers were also able to produce extremely large area, uniform monolayer graphene[78].

It has also been shown that uniformity in multi-layer graphene can be achieved by controlling carbon dose, anneal temperature and hydrocarbon precursor pressure[79]. Also, by increasing hydrogen concentration a uniform 2-3 layer graphene film was produced[80].

The characteristics listed lend themselves to the application of graphene in an x-ray detector window. X-ray detector windows are thin, highly x-ray transparent membranes which form an airtight seal. Silicon based detectors must be cooled in a vacuum, and contamination will destroy them. Therefore, an x-ray detector window must withstand at least one atmosphere of differential pressure and be leak tight. Also, because of low atomic weight, carbon membranes can transmit more x-rays than other materials [20, 48]. The diameters spanned by these membranes can be up to ~10 millimeters. However, windows used for microanalysis typically incorporate a membrane support lattice to enable extremely thin membranes to span these large areas. This still requires the thin membrane to span areas with dimensions on the order of hundreds of microns. Single layer graphene is not able to span these dimensions, but MLG has been shown to span these large dimensions[73]. Measuring the thickness uniformity of these different films after being suspended has not been explored in the literature.

Here we report growth and characterization of MLG films including x-ray transmission, thickness, thickness uniformity characterization, and burst pressure. Growths were performed on nickel foils 100 μm and 25 μm thick. The grown films were then transferred to silicon structures of two designs. A larger 7.5 mm diameter MLG film was suspended on a ribbed x-ray window support structure and x-ray transmission testing was performed on this membrane. There was a

20% improvement of boron and carbon x-ray transmission versus a modern polymer x-ray detector window in an EDS system using this membrane. Films were also suspended over smaller rectangular holes (200 μm - 1 mm) for thickness characterization (using optical transmission) and burst pressure measurements. There were two types of observed spatial variations in the suspended membranes: attached disordered carbon and variation in the thickness of the MLG film. These variations depended on the thickness of the Ni foil, as well as the surface preparation of the Ni foil substrate. There was significantly more disordered carbon attached to MLG films grown on the 25 μm compared to the 100 μm thick Ni foils. The thickness variation of the MLG films was greater for nanotextured samples compared to microtextured samples.

4.2 Experimental Methods

4.2.1 Nickel foil polishing

100 μm and 25 μm thick nickel foils were measured prior to surface preparation using a micrometer. The foils were within +/- 2 μm of nominal thickness. Some 100 μm thick foil was used for polishing, while 25 μm thick foil and some 100 μm thick foil was used for graphene growth without polishing. To polish foils, first, sections were cut in 10 mm x 10 mm squares. Polishing was done on an Allied Metprep polishing wheel with an Allied Diamond 3 μm lapping film. The film was rotated at 150 rpm with distilled water for coolant. The foil was held firmly by one end and a finger was used to press the foil against the lapping film with about 10 pounds of force. To get an even surface, the foil was pressed against the lapping film with one finger, while rolling the fingertip from side to side. This was repeated with both sides of the foil to polish both ends equally. Foils were polished until they appeared highly reflective. After

polishing, foils were measured with a micrometer and found to have a thickness within uncertainty of their original thickness.

4.2.2 Chemical Vapor Growth of MLG Film

Both cleaning and graphene growth for polished and unpolished nickel foils followed the same cleaning and growth process. Samples were placed sequentially in baths of de-ionized water, acetone, and IPA for 10 minutes each. They were dried on polyester wipes, then placed on a fused silica slide. The slide with nickel substrate was inserted in a 1" fused silica tube furnace. The system was pumped down below 10^{-3} torr and purged with Ar for 60 seconds. Following the purge, a flow of 50 standard cubic centimeters per minute (sccm) of H_2 and 10 sccm of Ar was introduced. The furnace was then heated up to 1050° C and held there for 15 minutes to anneal the nickel foil. 50 SCCM of CH_4 was introduced to begin growing graphene. After 13 minutes the flow of CH_4 was increased to 200 sccm for the final two minutes of growth. To rapidly cool the sample, the clamshell furnace lid was raised, and compressed air was manually blown onto the quartz tube in a sweeping motion for 5 minutes. After the furnace was cooled down, the flow of gases was stopped and there was a final purge of Ar for 60 seconds.

4.2.3 MLG Film Transfer to Silicon Support Structures

A PMMA (6% in anisole) coating was spin cast onto the top surface of the MLG coated nickel foils (see Figure 4.1). To remove the graphene from the backside of the nickel substrate the sample was flipped upside down and placed in an oxygen plasma etcher (Technics PlanarEtch II) at 250 W for 10 minutes. To remove the nickel, the sample was placed in a 0.1 g/mol $FeCl_3$ solution, with the PMMA coated graphene facing upwards. After 2-8 hours, depending on thickness of the Ni substrate, the sample was transferred to 3 successive DI water baths for 1-5 minutes each for rinsing. The PMMA supported graphene film was scooped out of

the DI water with a silicon support structure. The MLG on silicon support was placed in a furnace at 150 °C for > 12 hours to dry and anneal the PMMA to help the MLG film to adhere to the support (150° C exceeds the glass transition temperature of PMMA). Finally, a dry process[72] was used to remove the PMMA as to minimally disturb the suspended membrane. This dry process consisted of placing the sample in a 1" fused silica tube furnace at 350 °C while flowing H_2 (300 sccm) and Ar (300 sccm) through the tube for 12 hours.

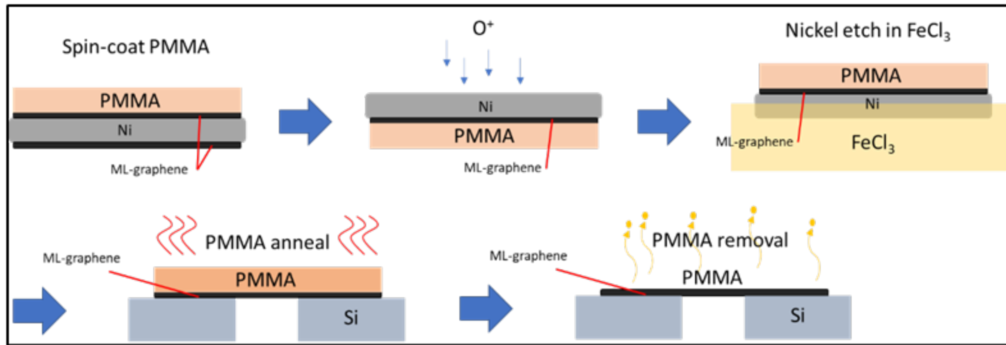

Figure 4.1 Transfer process for MLG on nickel foil. (a) Sample is spin coated with PMMA (b)The sample is flipped over and an oxygen plasma etch removes graphene from the backside (c) the sample is placed in a $FeCl_3$ solution, with the PMMA facing upwards, to etch away the nickel. The sample is placed in Di water baths to rinse it and is scooped out using an etched silicon support structure. The etched silicon support structure has rectangular through-wafer openings to create the suspended film regions. (d) Sample is then annealed at 150 °C for >12 hours to allow the MLG to adhere to the silicon surface. (e) PMMA is removed in a dry thermal process by placing the sample in a tube furnace flowing Ar and H_2 at 300 °C.

4.2.4 Atomic Force Microscopy

Atomic force microscopy (AFM) roughness measurements were performed using a Dimension 3100 upgraded to a Dimension V AFM in tapping mode, scanning 10 µm x 10 µm areas. Roughness was determined by calculating the root mean square of the height measurement. The qualitative maximum from the radial power spectral density function (PSDF) was used to calculate a one sided, one dimensional PSDF section, normalized to the maximum. Gwyddion 2.47 software was used to analyze the images.

4.2.5 Raman Spectroscopy

Raman measurements were made with a Renishaw inVia™ spectrometer, using a 532 nm 45 mW excitation laser. A spectrum from a silicon crystal was collected before the MLG films to calibrate. The wavenumber range was from 100-3500 cm^{-1}. Data was collected with a 50x objective for 100s with a laser power of 1%.

4.2.6 X-Ray Transmission

X-ray transmission data was collected by measuring a standard sample with EDS in a scanning electron microscope, with and without the MLG film in front of the x-ray detector. The standard sample had a mixture of B, C, N, O, Na, Al, Si and W elements. The beam energy was 15 kV, and spectra were collected for 20 minutes.

4.2.7 Optical Imaging

Images were captured with a CCD camera and Image J was used to analyze the images. Multiple images were taken with different levels of illumination of the same area. This was done because the camera did not have adequate dynamic range to measure transmission through open areas, areas with thin films, and those with thick films at the same level of illumination. Thin MLG film areas were measured relative to open areas under low illumination. Then, thick MLG film areas were measured relative to thin MLG film areas under high illumination. Relative transmission was then calculated.

4.2.8 Burst Testing

MLG films on support structures were placed in a burst testing fixture, where a positive pressure could be applied to the frontside using compressed nitrogen and an electronically controlled pressure regulator. An MFC measured the flow rate of gas through the film, indicating when the film broke and was no longer pressure tight.

4.3 Results

4.3.1 Ni Foil Results

AFM Characterization AFM images of unpolished and polished 100 μm thick nickel foil substrates prior to MLG growth are shown in Figure 4.2a and 4.2b. A polished sample had an RMS roughness of 11.5 nm, while an unpolished sample had an RMS roughness of 148 nm. Diagonal lines are shown on figures 4.2a and 4.2b, showing the profile lines that are graphed in Figure 4.2c. The unpolished sample has a long-range waviness, with valley-to-peak differences on the order of 100's of nanometers over a horizontal distance of 14 μm. The polished profile has valley to peak differences on the order of 10's of nanometers, but qualitatively has much more regular short-range roughness. A normalized radial one-dimensional radial Power Spectral Density Function (PSDF) section is shown in Figure 4.2d. There are several peaks at higher wavenumbers evident in the polished profile, not seen in the unpolished profile.

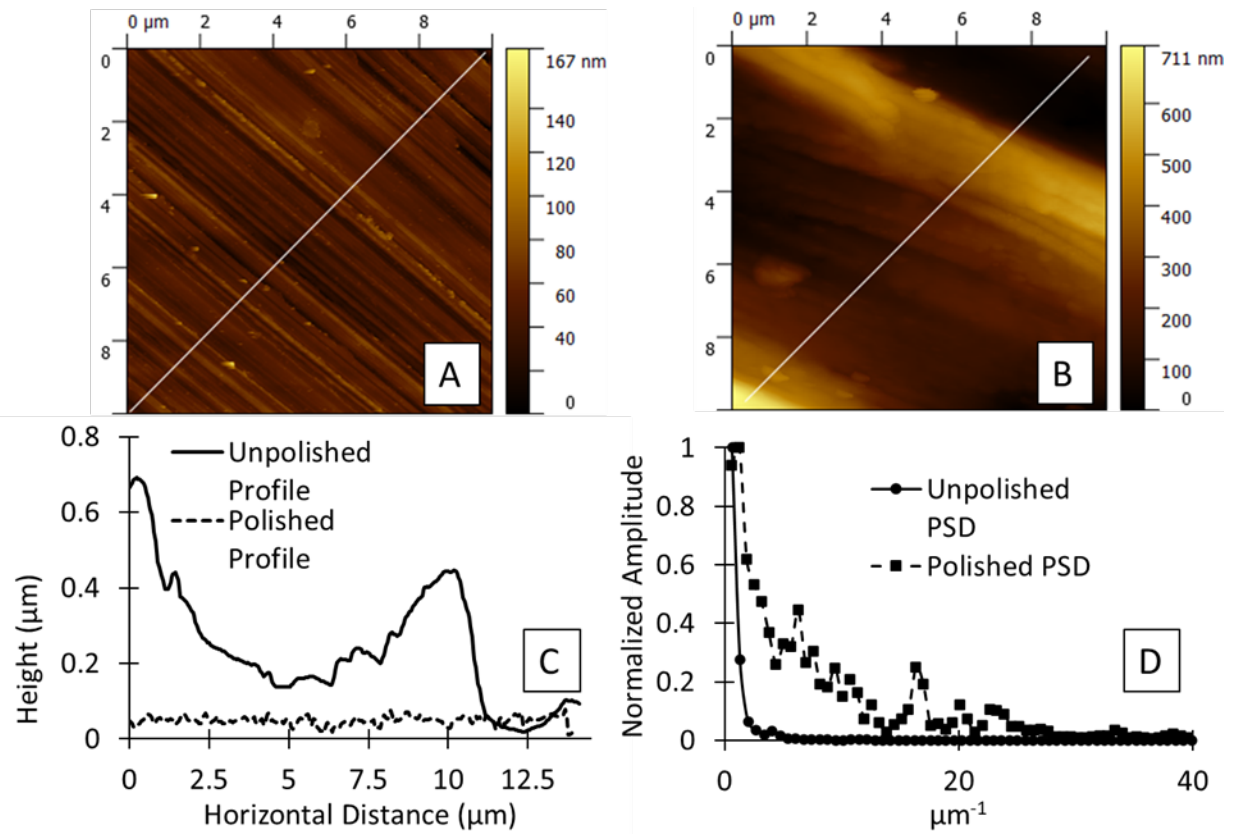

Figure 4.2 AFM characterization of nickel foil growth substrate (a) AFM measurement of a polished foil, the average rms roughness of the polished foils was 11.5 nm (b) The unpolished nickel foils showed an average rms roughness of 148 nm. (c) shows the difference in profile, with large magnitude over a longer horizontal distance exhibited by the unpolished foil (d) the power spectral density (PSD)shows several peaks at higher wavenumber for the polished foil, demonstrating roughness over a much shorter horizontal distance

4.3.2 MLG Films Results

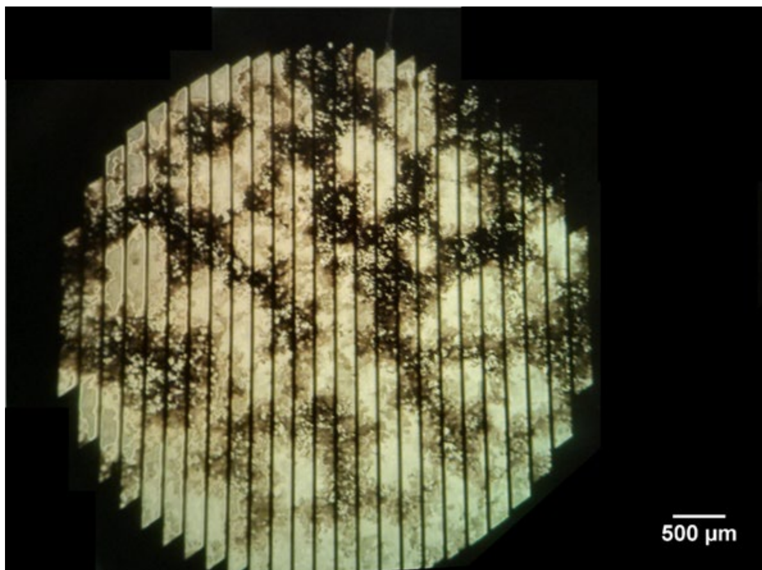

Figure 4.3 Optical transmission through MLG film suspended on a ribbed x-ray window support structure. MLG film was grown on an unpolished 25 µm thick Ni foil. The space between the ribs is 200µm. The darker areas in the film are from a disordered carbon film adhered to the backside of the MLG film. The disordered carbon was from carbon trapped in the bulk of the nickel foil that did not precipitate out during the growth or cooldown phases of the CVD process

In Weatherup et. al[81] it was shown that in the CVD graphene growth process on nickel, not all carbon that has been dissolved into the nickel foil will precipitate at the surface during cooldown. In situations where there is a large relative concentration of carbon a rapid cool down can leave disordered carbon in the bulk of the nickel foil. After removal of the nickel foils from the MLG films, this disordered carbon from the bulk nickel foil adhered to the MLG film in a non-continuous layer. Figure 4.3 is an optical micrograph of a suspended MLG film on a support structure; the film was grown on an unpolished 25 µm thick Ni foil. Note that for suspended graphene this is a particularly large total suspended area, spanning several millimeters with the aid of the support. There are darker areas visible where there is disordered carbon still attached to the MLG film. This disordered carbon film was not strongly adhered to the MLG film with most, but not all, delaminating during the transfer process. In one sample, the MLG film and

disordered carbon layer were stuck together initially, but during handling the MLG film partially slid off the underlying disordered carbon film. Figure 4.4 shows Raman spectra (normalized to the G peak) from the MLG film area and the disordered carbon area. An optical micrograph of these areas is shown in the inset of Figure 4.4, with the disordered carbon (dark area) layer next to the MLG film (light area). The disordered carbon spectra D peak is broad and about 50% in magnitude compared to the G peak. The spectrum from the MLG film shows a small D peak (< 10% in magnitude of the G peak), with a 2D peak about 25% in magnitude compared to the G peak. The 2D peak for the MLG film can also be fit between 2550 cm^{-1} and 2900 cm^{-1} using the Levenberg-Marquardt method with two Lorentzian functions (with a weighted sum of squared residuals of 609.145).

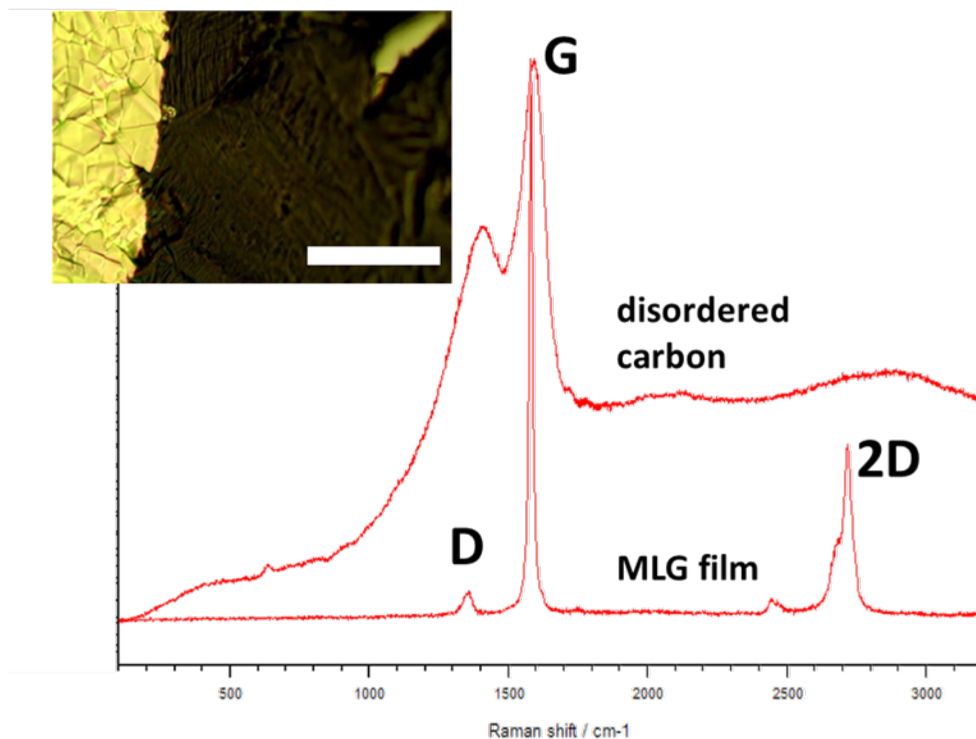

Figure 4.4 Raman Characterization of MLG film. The inset is an optical image from an MLG film (light area) that has partially slid off of an underlying disordered carbon film (dark area). Raman spectrum from disordered carbon has a broad large D peak at 1325 cm^{-1} (high disorder), and small broad 2D peak. MLG film spectrum has sharp G peak and small D peak. The 2D peak of the MLG film can be fit with 2 Lorentzian functions, typical of MLG films. (inset)Optical micrograph of the reflective MLG film next to the dark disordered carbon underlayer, scale bar is 30µm.

Optical Transmission Figure 4.5 contains optical transmission micrographs from MLG films prepared from different Ni foil types. The black, opaque areas in Figure 4.5 are covered by disordered carbon and are too dark to be measured. The lighter grey areas are the areas covered only by MLG films. There is variation in the grey areas coming from the variation of thickness of the MLG films.

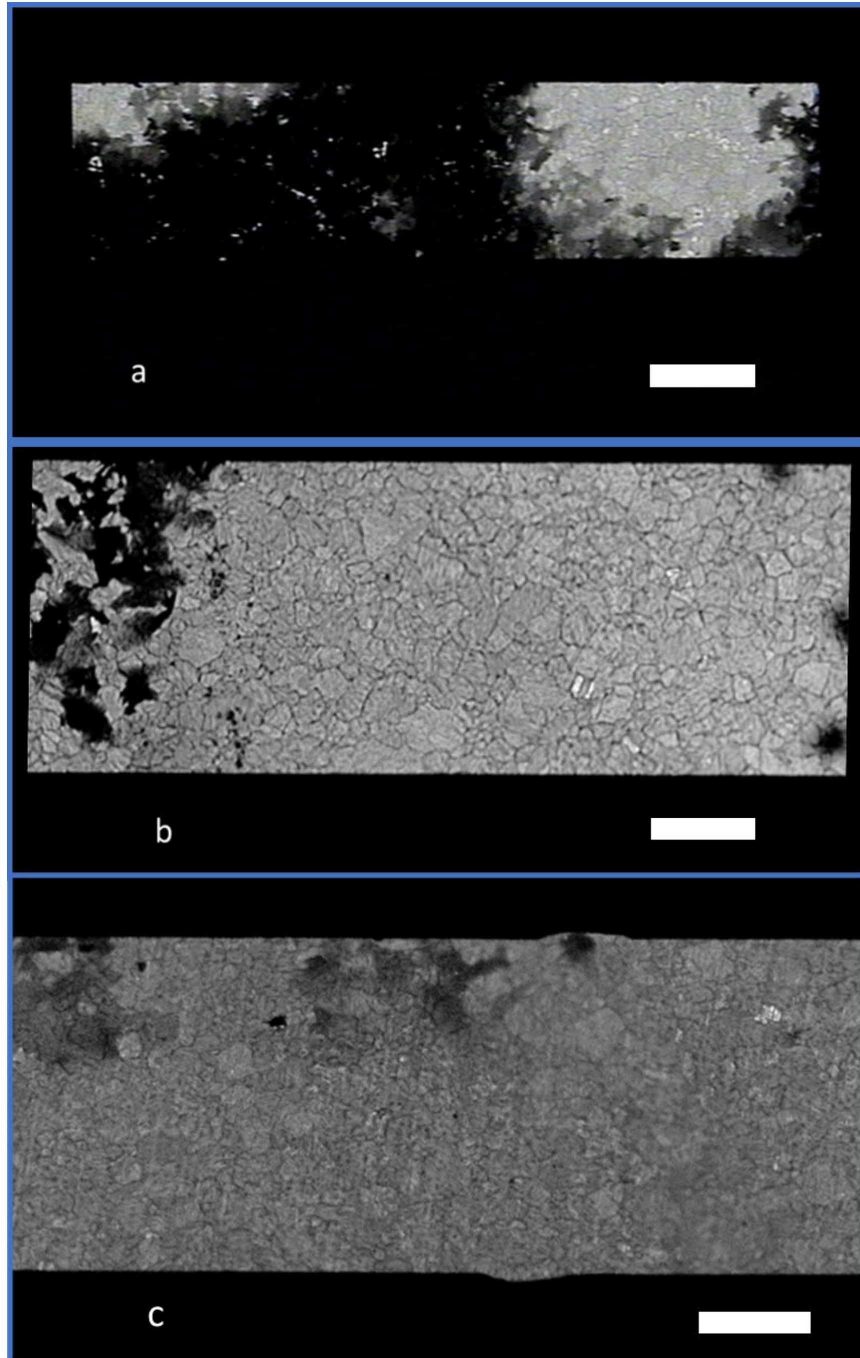

Figure 4.5 Optical transmission micrographs of MLG films suspended over rectangular holes in silicon. (a) was grown on an unpolished 25 µm thick Ni foil. (b) was grown on an unpolished 100 µm thick Ni foil and (c) was grown on a polished 100 µm thick Ni foil. Scale bars are 250 µm.

Figure 4.6a shows box plots and averages for area covered by disordered carbon for the different Ni foil types. The disordered carbon coverage for MLG films transferred from 100 µm foils was low (2% and 6% disordered carbon coverage, for polished and unpolished films). The

MLG films transferred from unpolished 25 μm thick Ni foils had 21% disordered carbon coverage. Zhu et al measured the optical transmittance of multilayer graphene films of different thicknesses[82] by stacking graphene layers and confirming with Raman spectroscopy. Equation 4.1 is the transmission of visible light through differing numbers of graphene layers from Zhu et al. In the equation α is the fine structure constant, T is the transmission of optical light through the film and N is the number of graphene layers, assumed to be 0.334 nm thick.

$$T = (1 + 1.13\pi\alpha N/2)^{-2} \tag{4.1}$$

Figure 4.6b shows the mean thickness of samples for each foil type. To quantify the thickness variation within each sample, the standard deviation of thickness for each sample, divided by the mean thickness for that sample was calculated. Figure 4.6c shows this normalized standard deviation of thickness within each sample. Table 4.1 summarizes the results.

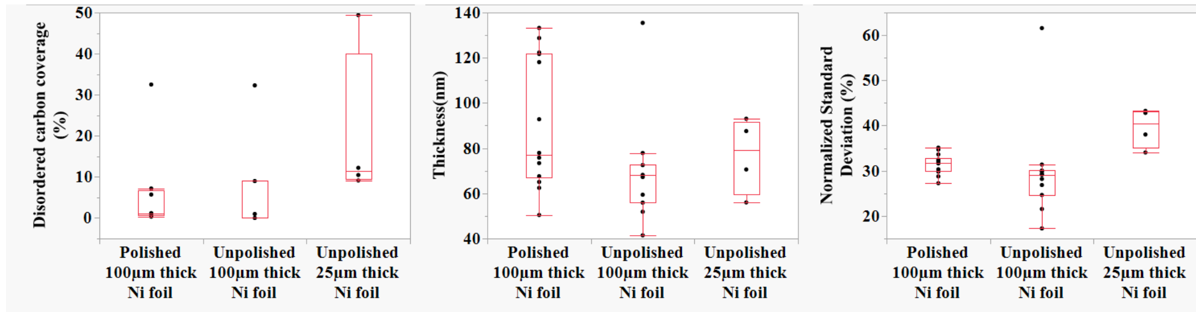

Figure 4.6 MLG film statistics box plots(red). Each point represents a different MLG film suspended over a rectangular hole. (a) The % area of the film that is covered by carbon film too thick to measure, assumed to be disordered carbon. (b) The mean thickness of each sample. (c) The standard deviation of the thickness within each sample, normalized by that sample's mean thickness.

Table 4.1 Summary of thickness results from optical transmission testing.

Ni Substrate Type	Thickness(nm)	Std Dev Thickness(nm)	Normalized Standard Deviation (%)	Number of Samples
Unpolished 100µm thick Ni foil	70.1	24.1	30.0	11
Polished 100µm thick Ni foil	89.8	28.8	31.4	14
Unpolished 25µm thick Ni foil	76.8	16.8	39.5	4

X-Ray Transmission

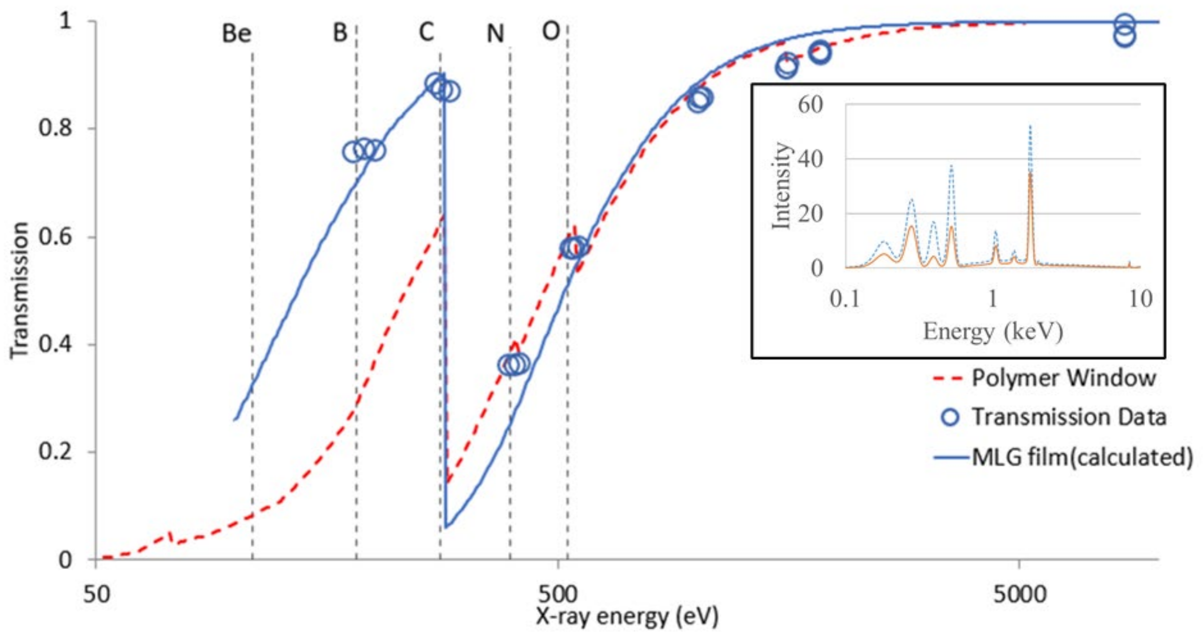

Figure 4.7 X-ray transmission of MLG film and comparison materials. The solid line is the fitted transmission of the MLG film, the dashed line is the transmission of an advanced polymer film for comparison. EDS spectra were gathered in a SEM from a sample with known composition. The open circles are calculated transmission values at energies corresponding to fluorescence peaks from elements in the sample. The transmission curve was fitted using data from CXRO database. The inset contains EDS spectra from a sample of known composition, with and without the MLG film in front of the detector. This data was used to calculate the transmission of the MLG film in the main graph.

Figure 4.7 shows the x-ray transmission of an MLG film grown on an unpolished 25 µm thick Ni foil. This was calculated by taking the ratio of two spectra of a standard sample. One spectrum was collected with the film on the support structure in front of the EDS detector, and

one with only the EDS detector. This produced the two spectra in the insert of Figure 4.7. The transmission of the film at the 3 channels closest in energy to the emission of elements in the sample being scanned by the EDS detector was used. The open circles in in Figure 4.7 show the calculation of the spectra multiplied by the open area of the support structure. These points were used to fit the full x-ray transmission curve using data from the Center for X-Ray Optics at Lawrence Berkeley National Laboratory. This fit indicated that the MLG film was 188 nm in effective thickness. This thickness includes the disordered carbon that covered some areas as can be seen in Figure 4.3.

Burst Pressure The burst pressure of each film compared to its thickness and width is shown in Figure 4.8. Most samples burst between 1 and 4 psi. There was one sample that broke at a relatively higher pressure compared to the other samples. The bursting pressure was not dependent on either the thickness of the MLG film or the width of the silicon support opening.

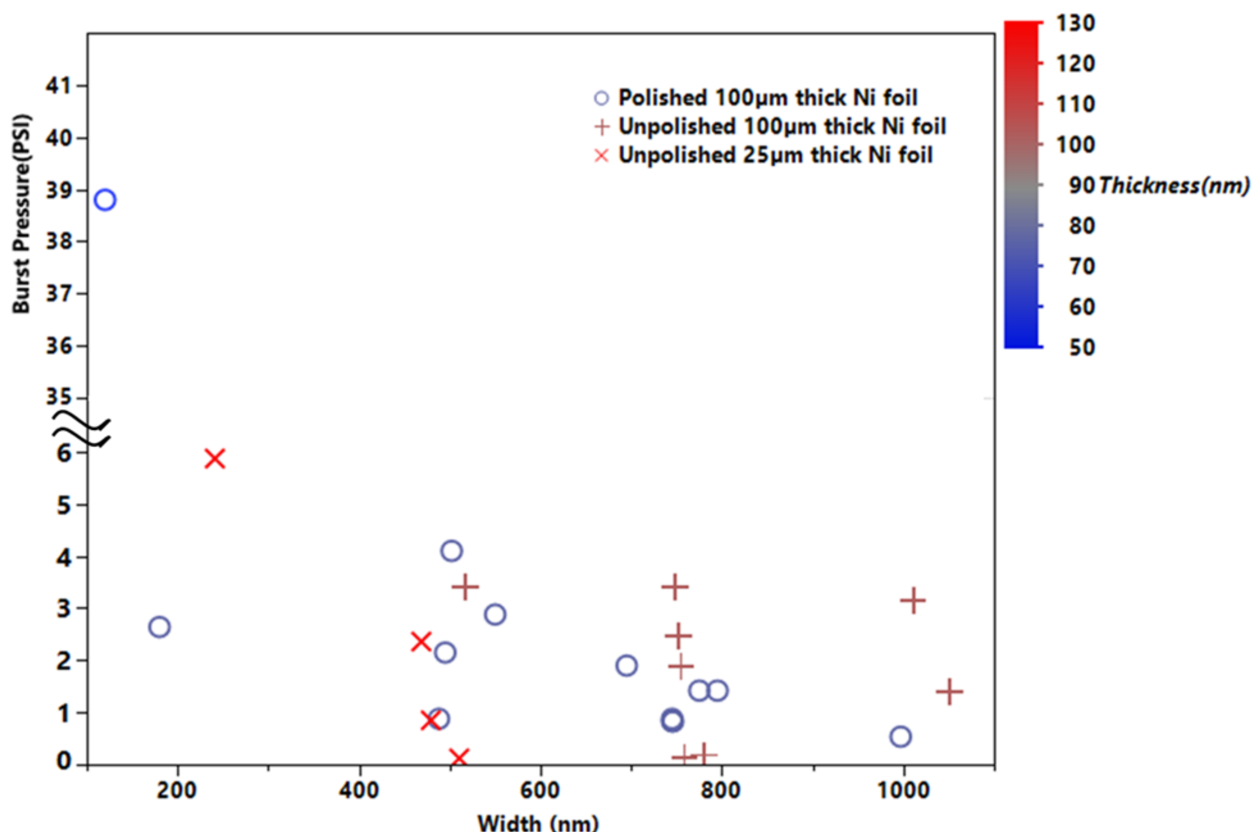

Figure 4.8 Burst pressure of suspended MLG films. Burst pressure of films of varying thickness suspended over rectangular holes in silicon supports. Films were grown on polished and unpolished Ni foils of 25 and 100 μm thickness. Most samples burst below 6 PSI with no clear correlation of burst pressure to width of the suspended window, or thickness of the MLG film. One sample burst at a much higher pressure than the other samples.

4.4 Discussion

Polishing the Ni foil reduced the long range (~10 μm) waviness, as can be seen in Figure 4.2c. However, this introduced an increase in short order roughness (< 1 μm), seen in the higher wavenumber peaks of the PSDF in Figure 4.2d.

The Raman results of the MLG film show a small D peak indicating low disorder. The ratio of the 2D peak to G peak of about 25%, as well as the 2D peak being fit by 2 Lorentzian functions is typical of many-layer graphene and highly ordered pyrolytic graphite[83]. The disordered carbon film that adhered to some areas of the MLG films is typical of CVD graphene growth on Ni when the substrate becomes saturated[81].

Optical transmission micrographs showed some differences and some similarities between MLG films grown on the different nickel foil conditions. Sample sizes were small (less than 5 samples in the unpolished 25 µm Ni foil group), so more data is needed to gain confidence in the conclusions, but some observations can be made. Films grown from the 25 µm foil had a 14% higher average amount of disordered carbon coverage than films grown on 100 µm foils. A p-value of 0.8 was calculated when comparing the mean amount of disordered carbon coverage in a one-way t-test between the films grown on 25 µm thick foils and those grown on polished 100 µm thick foils. Also, a p-value of 0.07 was calculated when comparing the 25 µm thick foils with unpolished 100 µm thick foils. These p-values are not conclusive in showing a difference in disordered carbon coverage, but they show a likely difference in the mean amount of disordered carbon on MLG films grown on 25 µm thick foils, and those grown on 100 µm thick foils. Polishing the nickel foil surface did not show any significant difference in MLG film disordered carbon coverage. The distributions of mean thicknesses did show a significant difference in the average thickness between MLG films grown on polished and unpolished 100 µm thick Ni foils, with a one-way t-test having a p-value of 0.04 and unpolished 100 µm thick Ni foils being on average thinner by 10 nm. Also, the standard deviation of mean thickness was 4 nm higher for MLG films grown on polished 100 µm thick Ni foils vs unpolished 100 µm thick Ni foils, with an interquartile range difference of 55 nm vs 17 nm. These results suggest that polishing the Ni foils increased the average thickness of MLG films and increased the variation in mean thickness. Other comparisons for mean thickness were not significantly different. The normalized standard deviation, which shows the thickness variation within a sample, was significantly higher for MLG films grown on unpolished 25 µm thick Ni foil. MLG films grown on polished 100 µm thick Ni foils had a normalized standard deviation 8 nm lower, with a p-

values of < 0.01. Also, MLG films grown on unpolished 100 µm thick Ni foils had a normalized standard deviation 9 nm lower with a p-value of 0.06. Thus, it is likely that MLG films grown on 100 µm thick Ni foils had less thickness variation within a sample.

Figure 4.7 shows a significant improvement (~20%) in x-ray transmission in the x-ray fluorescence energy regime of boron and carbon elements compared to a modern polymer window. The disordered carbon contributed to the calculated thickness of the MLG film with the fitted thickness approximately 100 nm thicker than the average thickness of the graphene film. The MLG films were shown to sustain a positive pressure. The films burst mostly below pressures of 6 psi, with one sample able to withstand much higher pressures. The films grown on 25 µm thick Ni foil had the highest amount of coverage of disordered carbon, but this did not result in higher burst pressures, as can be seen in Figure 4.8. This is expected, as nonuniform films will generally experience the highest amounts of stress in the thinnest regions. The large variation in burst pressure and the insensitivity to film thickness or suspension width would indicate that burst pressure is strongly dependent on defects. All films with burst pressure measurements were continuous (contained no holes or gaps) as observed in the optical microscope.

4.5 Conclusion

The MLG films showed a 20% improvement in x-ray transmission for lower energy x-ray fluorescence from B and C elements compared to a modern polymer window. MLG films were prepared from nickel foils with different surface preparations and different thicknesses using CVD. Disordered carbon on average covered more area on films grown with 25 µm thick foil Ni compared to 100 µm thick foil. MLG film normalized within sample thickness uniformity was 40% when prepared with unpolished 25 µm thick Ni foils, and 30% for unpolished and polished

100 µm thick Ni foils. The MLG films were suspended over holes with widths ranging from 100 µm's to 1 mm. The MLG films were shown to sustain a positive pressure, and bursting below pressures of 6 psi, although one sample was able to withstand much higher pressures. MLG films show promising signs for x-ray detector windows but need further development. Burst test results show that some positive pressure (around 4 psi) could be applied to MLG films over large areas, which is lower than the requirements of commercial x-ray windows (>1 atm). Our results suggest that higher thickness uniformity of MLG films and lower coverage of disordered carbon contamination are achieved by using thicker (~100 µm) Ni foil substrates that are smooth on the nanoscale.

Chapter 5 Brief Preliminary Studies

5.1 Alternate Formation Methods for Many-layer Graphene Films

Suspending MLG films on silicon support structures and sub millimeter sized rectangular holes, and then burst testing them, showed that these films could be transferred and form an airtight seal. However, most of these films broke at lower pressures than are necessary for x-ray detector windows. While burst testing these films, it was observed that these films were bursting at several small regions but most of the film would be intact even as pressures approached 1 atm (see Figure 5.1)

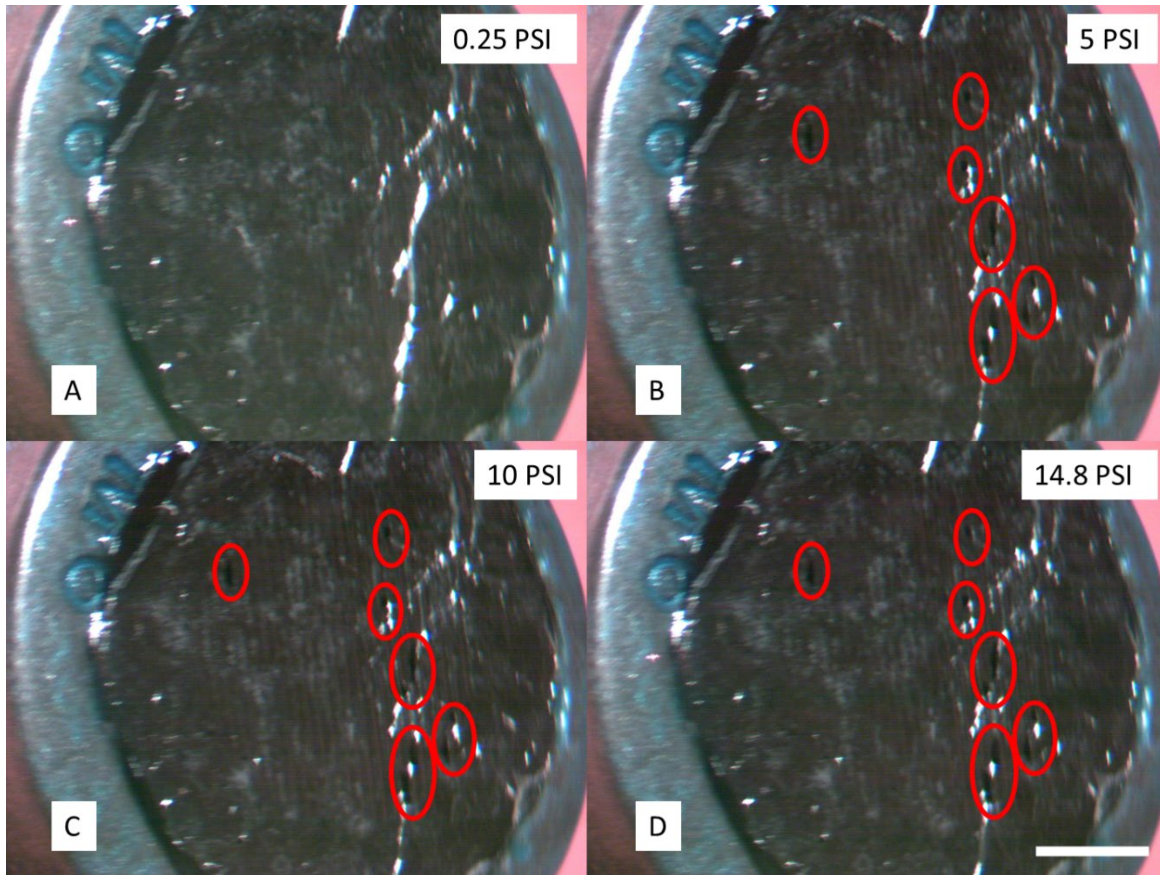

Figure 5.1 Images of MLG film as it was bulge tested. A-D show holes appear as pressure was increased, but no catastrophic failure

The observation of small, localized failures, rather than catastrophic failure, lead to the assumption that small defects were driving failures, rather than the intrinsic strength of the MLG films. This lead to investigating methods to improve uniformity the MLG films by improving the CVD growth process.

5.1.1 Templated Growth

In past work, carbon infiltrated carbon nanotubes[84] were investigated as a novel MEMS material. After growing a forest of carbon nanotubes using a growth catalyst on a substrate, an additional CVD process step was added to fill the forest with additional carbon. This process caused multiwalled carbon nanotubes to have additional layers grown with a pseudo epitaxial growth of sp^2 carbon. This can be seen in the lattice fringes in Figure 5.2.

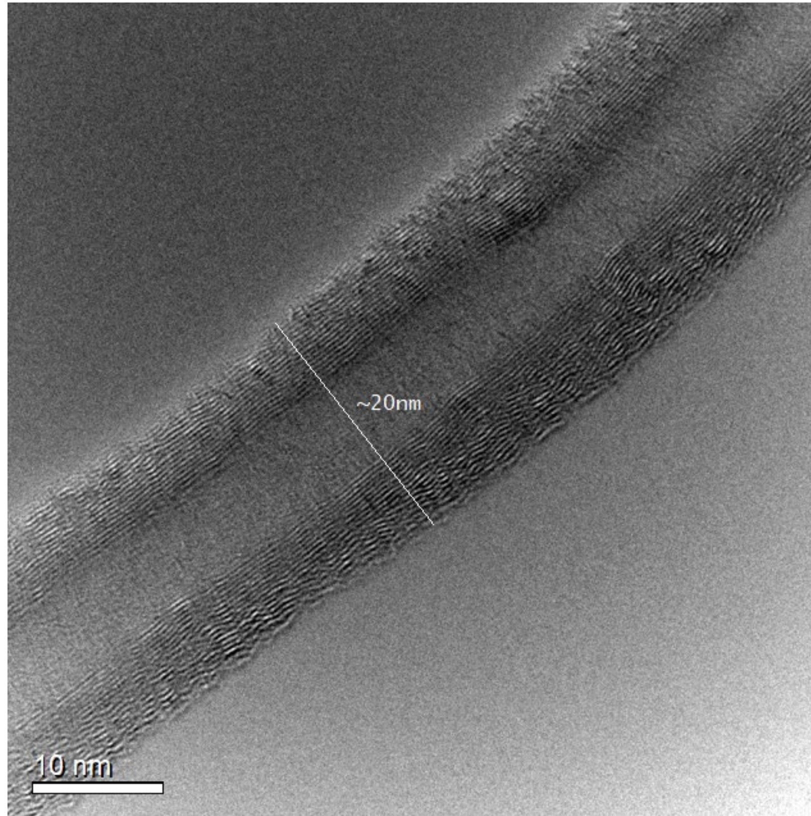

Figure 5.2 TEM image of multiwalled carbon nanotube

It was hypothesized that growing graphene layers on top of a single layer of graphene could create multilayer graphene that would be more uniform in thickness, in a similar manner to how additional graphitic carbon layers were grown on carbon nanotubes. Single layer graphene on silicon was obtained from Graphene Supermarket, and a similar process to depositing carbon on nanotubes was used to try and grow additional graphene layers. This was done by placing the sample into a 1” fused silica tube furnace, introducing a flow of ethylene and hydrogen at atmospheric pressure, and heating the furnace to 900 ° C. The resultant film was imaged using SEM (Figure 5.3).

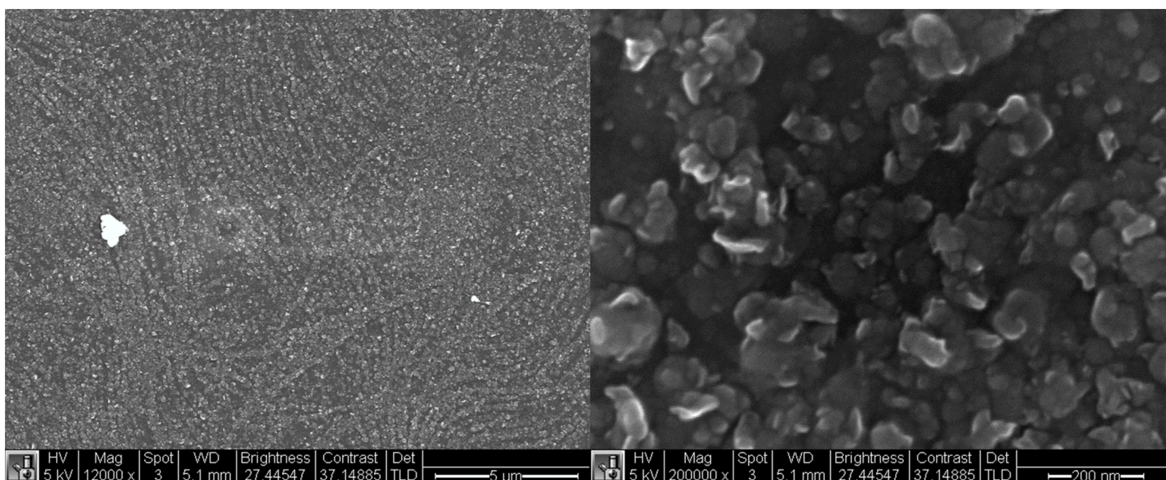

Figure 5.3 SEM image of carbon film growth on top of single layer graphene

The film exhibited a grainy look, with 50-150 nm sized features. The film was also very brittle, with portions of the film cracking when the sample was handled with tweezers. EDS was collected and showed only C, O, and Si present (Figure 5.4).

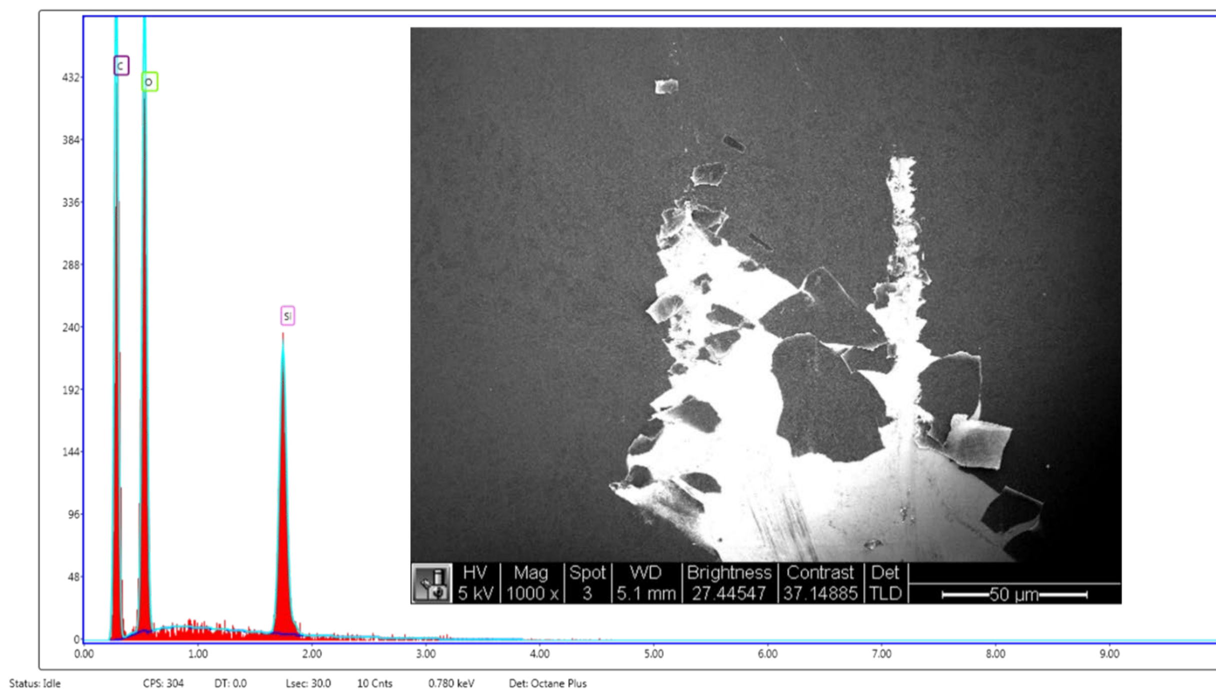

Figure 5.4 EDS spectra of carbon film, inset is region of film that cracked

Using a cracked region, it was possible to collect an image of the films cross section to estimate the thickness between 23 and 74 nm (Figure 5.5).

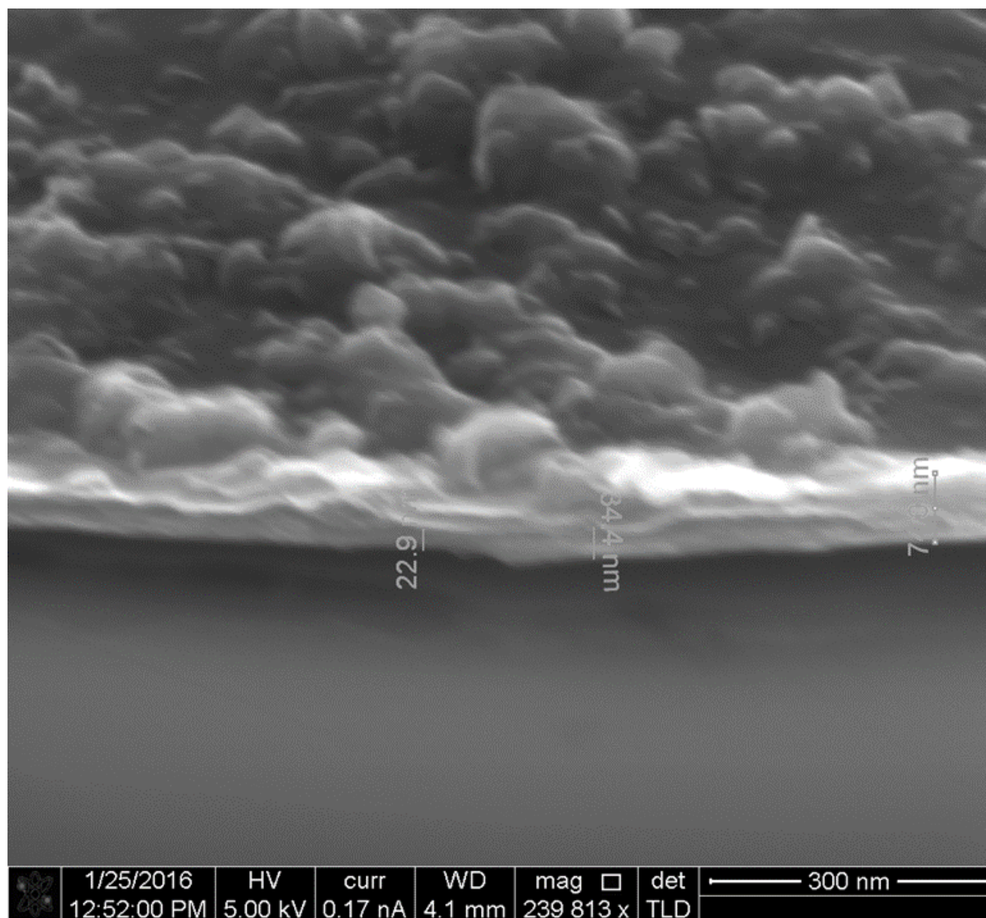

Figure 5.5 Cross section of carbon film growth on top of single layer graphene.

Using KOH to etch the silicon substrate, the carbon film was released and suspended on a washer with ~1mm diameter hole. Raman spectroscopy was collected, showing the presence of a large D peak at ~1350 cm^{-1}, indicating a high amount of disorder (Figure 5.6).

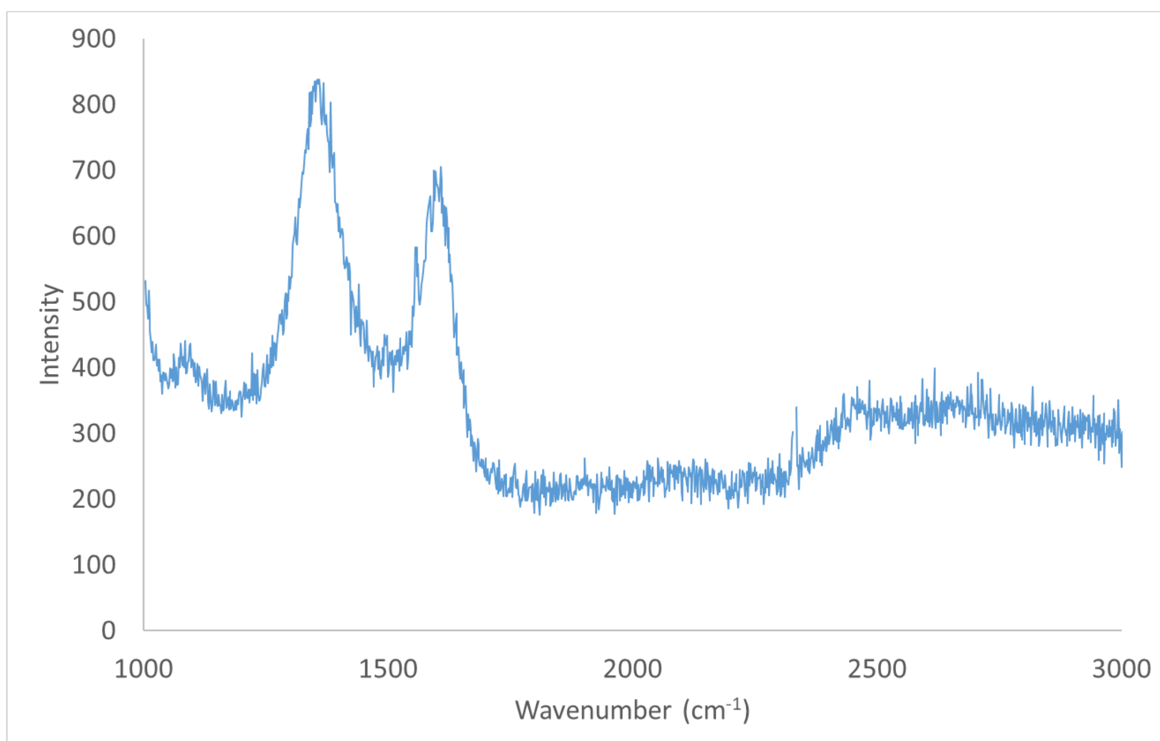

Figure 5.6 Raman spectra from carbon film grown on single layer graphene

In order to check if the initial graphene layer was being damaged by the CVD process, a graphene sample on silicon was tested with a modified CVD process. The sample was placed in the tube furnace, and only hydrogen was introduced while the furnace was heated to 900 ° C. Raman spectra was collected from this sample before and after heating, and considerable damage was seen by the formation of a D peak in the spectra (Figure 5.7).

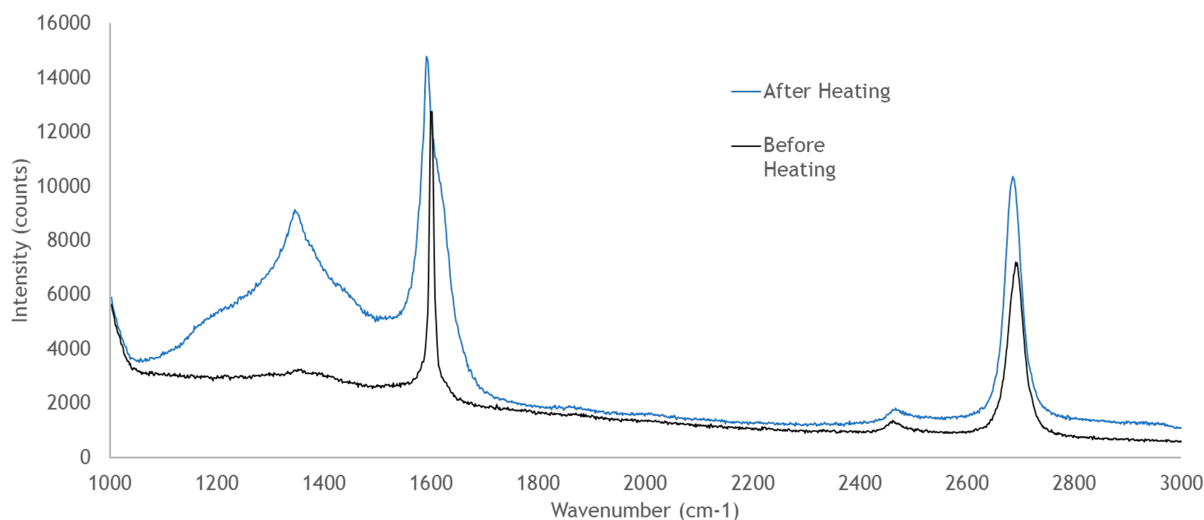

Figure 5.7 Raman Spectra from a single layer graphene sample on Si substrate before and after heating in hydrogen environment

Further investigation of literature showed that positive results had been seen using ethanol and hydrogen, and this is future work that could be done to develop a better MLG film[85].

5.1.2 Single Crystal Ni

Iwasaki[78] demonstrated large area single crystal graphene growth using single crystal nickel. Single crystal nickel was deposited on an MgO substrate by use of a buffer layer. A 50 nm film was first sputtered while the MgO substrate was heated to 300 °C. This suppressed twin formation in the Ni film, but the film was polycrystalline with small domains. In the second step, a 100 nm thick Ni film was sputtered onto the MgO substrate while it was heated to 600 ° C. This layer also did not have twins due to its deposition on top of the initial Ni buffer layer. After annealing at 800° C, a single crystal Ni surface was formed. In this way, thin single crystal nickel films were deposited on MgO substrates. Using CVD growth techniques like those in Chapter 4, it would be possible to grow high quality multilayer graphene films on the single crystal Ni films.

At the time, there were no sputtering systems at BYU that could sputter while heating a substrate to 600 ° C. A modified DV-602A Denton Vacuum sputtering system was brought into the labs and brought to a working condition (Figure 5.8). A nickel target was fabricated, and timed nickel depositions were performed on silicon wafers to measure the deposition rate.

Figure 5.8 Modified DV-602A Sputtering system

Once a deposition rate was determined, a single crystal MgO substrate was used to perform the two-step deposition process. During deposition, Cu was also sputtered onto the surface. This was caused by the lack of a dark space shield, which was added for later testing. The initial Ni and Cu deposition was removed from the MgO substrate by etching in a $FeCl_3$ solution. The two-step sputtering process was repeated, and this time a pure nickel film was deposited. After annealing at 800 ° C the film remained polycrystalline. Further annealing was done at 800° C for 4 days, but the film remained polycrystalline. The Ni film was etched off and

the MgO surface was inspected using orientation imaging microscopy (OIM) to check if there were differently orientated domains in the MgO substrate, which could explain why single crystal nickel films were not formed. OIM showed no domains of other orientations, but that the surface was now scratched. (Figure 5.9).

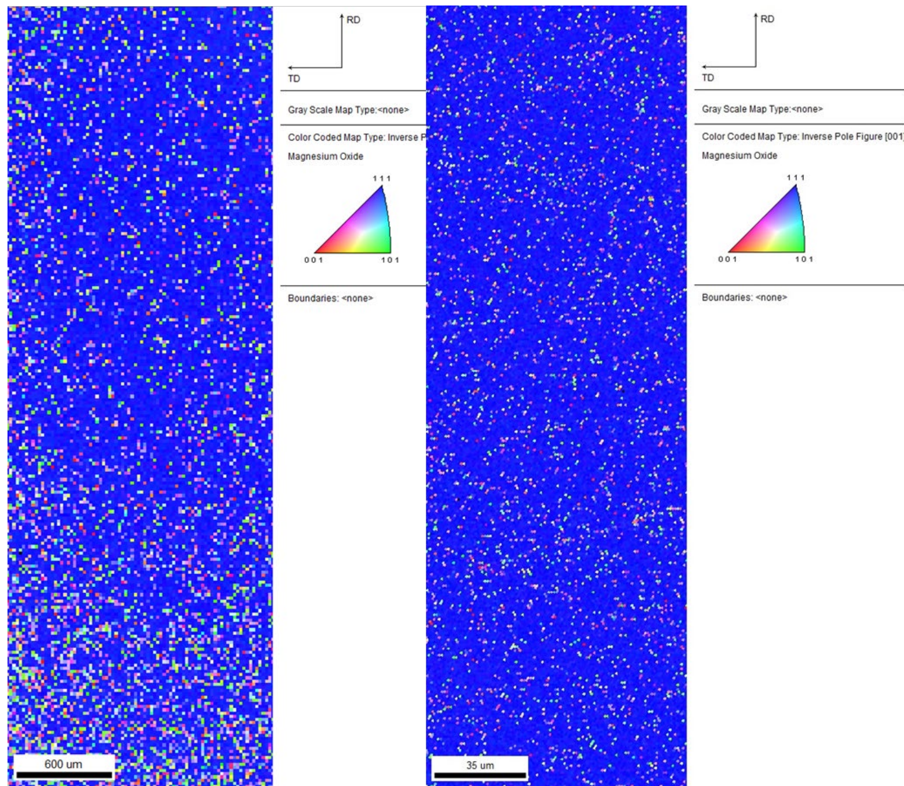

Figure 5.9 OIM image of MgO substrate after etching Ni/Cu film at 2 different magnifications

The etching solution was then shown to contain some precipitates that scratched the MgO surface. This is a possibility for future work, with a manufacturable process for producing thin single crystal Ni films that can be used for high quality MLG film growth.

Chapter 6 Conclusion and Future Work

This work has advanced understanding in the use of amorphous carbon and graphene in x-ray detector windows. As the study of low atomic number elements becomes more widespread, such as the study of lithium in energy storage research, the ability to quickly map out and detect low atomic number elements using EDS in microscale and nanoscale samples is becoming more critical. Carbon has allotropes that are especially suited for thin protective coatings, as well as some that have among the highest strength of any material. This makes carbon thin films valuable for use as a component of x-ray windows, or as the main membrane on a support structure.

Characterizing sputtered amorphous carbon for use as a corrosion barrier in an x-ray detector window opens up the use of thin metal films. Because many metal films are susceptible to oxidation, depositing them in thin layers makes them vulnerable to failing as a pressure and diffusion barrier. Sputtered amorphous carbon can be used, even in very thin depositions, to protect these thin metal layers and keep film stacks with thin layers intact for use in x-ray detector windows.

X-ray detector windows are subjected to mechanical stress, and since they are composed of thin films, candidate membranes are not suitable for conventional pull testing to measure strength. Bulge testing is a key method of quantifying mechanical properties. Strength is measured as films are tested in the same manner of their operation, with a uniform pressure applied to one side of a film. From this work it is seen that building a bulge tester is possible using mostly off the shelf components. This device is capable of measuring films with a rough or opaque coating using diffuse reflection, as well as measuring films that are smooth and some that

are semi-transparent, by using specular reflection. In addition, this device can also apply pressure to either side of a sample, simplifying measurements of samples that have support structures while allowing them to be pressurized up to 100 psi, which is not possible with a vacuum setup. The LabVIEW programs for this device make testing automated and analysis semi-automated. In addition to measuring mechanical properties, this bulge tester was combined with light microscopy, so real-time monitoring and visual evaluation of thin films can be done as pressure is applied.

The combination of bulge testing and light microscopy can lead to valuable future work when combined with high-speed photography. A high speed camera was used, in combination with the bulge tester, to capture the bursting of films made from smooth, thin, carbon nanotube composite sheets[86]. This first testing was able to capture the burst of this film over a few frames while recording at > 500 frames per second, while using the bottom pressure setup. There are complications from the size of the sample, limited optical access because of the laser displacement sensor, and the lighting needed for good imaging of the sample. When imaging light was increased too much it interfered with the laser displacement sensor, and it was difficult to get lenses close enough to the sample to get a good image. Using the top pressure setup, and some filters to isolate the displacement sensor's wavelength from the light used to illuminate the sample, significant improvements could be made to imaging at higher frames per second, with greater resolution. This would allow for observations of how films fail, whether slowly over localized regions, or quickly in catastrophic failures, aiding in modeling and design of future films.

Sputtered amorphous carbon is not strong enough to become an x-ray detector window on its own, but graphene, another allotrope of carbon, is extremely strong and able to span dimensions

on the order of microns while only being a single layer thick. Many-layer graphene films have been able to span millimeter size holes but had yet to be characterized for burst pressure and thickness uniformity. MLG films were created using a combination of methods from the literature. MLG films were suspended over relatively large 10 mm diameter support structures. The support structures had a horizontal support spacing of ~200 µm, and the supported MLG films were able to withstand some positive pressure. As these films were pressurized, most films were able to withstand up to one atmosphere of pressure without catastrophic failure, only failing in small, localized regions. MLG films were shown to have good x-ray transmission characteristics, but most of the films were not able to sustain the pressure necessary to work as x-ray detector windows. Improving these MLG films is critical to their success as x-ray detector windows and some methods to improve their uniformity were briefly investigated.

The first attempts to grow additional layers of graphene on top of existing layers (See Chapter 5) created amorphous carbon and not additional graphene layers. In Negishi et al.[85], controlled growth of additional graphene layers on top of existing graphene, while suppressing the growth of amorphous carbon, was demonstrated. Researchers used ethanol in their CVD process, and this, along with the right temperature and hydrogen flow rate, was believed to etch away any growth of amorphous carbon but allow the growth of additional graphene layers on top of existing graphene. This has yet to be replicated at BYU and could introduce a method for higher quality MLG films that could better withstand higher pressures across the entirety of the film.

In chapter 4 it was demonstrated that modifying the surface of a nickel substrate can change the amount of amorphous carbon that adheres to the backside. Chapter 5 discussed initial efforts of fabricating a single crystal nickel thin film, using previous work[78]. Additional MgO substrates

are available, and with the availability of the sputtering system at BYU that can now heat substrates up to 600 °C, it is possible to continue to characterize and grow nickel films to produce a single crystal film ready for graphene growth. The initial work from Iwasaki et al. focused on single layer graphene growth, and so growing thicker graphene films with many layers has yet to be explored.

Using the methods developed in this work MLG films can be fabricated and suspended over support structures designed for x-ray detector windows. Although the MLG films developed here were not able to withstand the pressures necessary to function as x-ray detector windows, most films only failed over small regions. With the possibilities for improving the uniformity of MLG films briefly studied here, a graphene based x-ray detector window is a promising possibility.

Bibliography

1. J. I. Goldstein, D. E. Newbury, J. R. Michael, N. W. Ritchie, J. H. J. Scott and D. C. Joy, *Scanning electron microscopy and X-ray microanalysis*. (Springer, 2017).
2. H. James, (Google Patents, 1947).
3. V. Cosslett and P. Duncumb, Nature **177** (4521), 1172-1173 (1956).
4. R. Fitzgerald, K. Keil and K. F. Heinrich, Science **159** (3814), 528-530 (1968).
5. J. Blankenship and C. Borkowski, IRE Transactions on Nuclear Science **9** (3), 181-189 (1962).
6. E. Hubbard, IEEE Transactions on Nuclear Science **15** (4), 14-20 (1968).
7. P. Lechner, S. Eckbauer, R. Hartmann, S. Krisch, D. Hauff, R. Richter, H. Soltau, L. Strüder, C. Fiorini and E. Gatti, Nuclear Instruments and Methods in Physics Research Section A: Accelerators, Spectrometers, Detectors and Associated Equipment **377** (2-3), 346-351 (1996).
8. B. L. Henke, E. M. Gullikson and J. C. Davis, Atomic data and nuclear data tables **54** (2) (1993).
9. M. Ohring, *Materials science of thin films*. (Elsevier, 2001).
10. C. Lawrence, The Physics of fluids **31** (10), 2786-2795 (1988).
11. G. Binnig, C. F. Quate and C. Gerber, Physical review letters **56** (9), 930 (1986).
12. N. Jalili and K. Laxminarayana, Mechatronics **14** (8), 907-945 (2004).
13. G. G. Stoney, Proceedings of the Royal Society of London. Series A, Containing Papers of a Mathematical and Physical Character **82** (553), 172-175 (1909).
14. G. C. Janssen, M. Abdalla, F. Van Keulen, B. Pujada and B. Van Venrooy, Thin Solid Films **517** (6), 1858-1867 (2009).
15. B. A. Carter, D. B. Williams, C. B. Carter and D. B. Williams, *Transmission Electron Microscopy: A Textbook for Materials Science. Diffraction. II*. (Springer Science & Business Media, 1996).
16. R. F. Egerton, Reports on Progress in Physics **72** (1), 016502 (2008).
17. E. Smith and G. Dent, (2005).
18. A. Gupta, G. Chen, P. Joshi, S. Tadigadapa and P. Eklund, Nano letters **6** (12), 2667-2673 (2006).

19. A. C. Ferrari and J. Robertson, Physical review B **61** (20), 14095 (2000).

20. J. Rowley, L. Pei, R. C. Davis, R. R. Vanfleet, S. Liddiard, M. Harker and J. Abbott, Journal of Vacuum Science & Technology A: Vacuum, Surfaces, and Films **34** (5) (2016).

21. J. Rowley, K. Berry, R. Davis, R. R. Vanfleet, S. Cornaby, M. Harker and R. Creighton, Microscopy and Microanalysis **21** (S3), 2005-2006 (2015).

22. B. Bhushan, (1990).

23. V. Elinson, V. Sleptsov, A. Laymin, V. Potraysay, L. Kostuychenko and A. Moussina, Diamond and related Materials **8** (12), 2103-2109 (1999).

24. M. Fung, K. Lai, C. Chan, I. Bello, C. Lee, S. Lee, D. Mao and X. Wang, Thin Solid Films **368** (2), 198-202 (2000).

25. S. Vasquez-Borucki, W. Jacob and C. A. Achete, Diamond and related materials **9** (12), 1971-1978 (2000).

26. H. Kodama, M. Nakaya, A. Shirakura, A. Hotta, T. Hasebe and T. Suzuki, new Diamond and Frontier carbon Technology **16** (2), 107-119 (2006).

27. H. Kodama, A. Shirakura, A. Hotta and T. Suzuki, Surface and Coatings Technology **201** (3-4), 913-917 (2006).

28. A. Ogino and M. Nagatsu, Thin Solid Films **515** (7-8), 3597-3601 (2007).

29. Y. Show, Surface and Coatings Technology **202** (4-7), 1252-1255 (2007).

30. J. Li, C. Gong, X. Tian, S. Yang, R. K. Fu and P. K. Chu, Appl Surf Sci **255** (7), 3983-3988 (2009).

31. S.-m. Baek, T. Shirafuji, N. Saito and O. Takai, Japanese Journal of Applied Physics **50** (8S1), 08JD08 (2011).

32. S. Mattioli, M. Peltzer, E. Fortunati, I. Armentano, A. Jiménez and J. M. Kenny, Carbon **63**, 274-282 (2013).

33. O. Polonskyi, O. Kylián, M. Petr, A. Choukourov, J. Hanuš and H. Biederman, Thin solid films **540**, 65-68 (2013).

34. W. Jin, K. Feng, Z. Li, X. Cai, L. Yu and D. Zhou, Journal of Power Sources **196** (23), 10032-10037 (2011).

35. D. Luo, M. Zhao, M. Xu, M. Li, Z. Chen, L. Wang, J. Zou, H. Tao, L. Wang and J. Peng, ACS applied materials & interfaces **6** (14), 11318-11325 (2014).

36. D. Luo, H. Xu, M. Zhao, M. Li, M. Xu, J. Zou, H. Tao, L. Wang and J. Peng, ACS Applied Materials & Interfaces **7** (6), 3633-3640 (2015).

37. V. Raman and K. Coffey, Applied physics letters **59** (25), 3244-3246 (1991).

38. N. Savvides and B. Window, Journal of Vacuum Science & Technology A: Vacuum, Surfaces, and Films **3** (6), 2386-2390 (1985).

39. B. Gupta and B. Bhushan, Thin Solid Films **270** (1-2), 391-398 (1995).

40. M. Puchert, P. Timbrell, R. Lamb and D. McKenzie, Journal of Vacuum Science & Technology A: Vacuum, Surfaces, and Films **12** (3), 727-732 (1994).

41. M. Stüber, S. Ulrich, H. Leiste, A. Kratzsch and H. Holleck, Surface and Coatings Technology **116**, 591-598 (1999).

42. C. Davis, Thin solid films **226** (1), 30-34 (1993).

43. J. Robertson, Diamond and related materials **2** (5-7), 984-989 (1993).

44. C. Jensen and R. Hoffman, Journal of Vacuum Science & Technology A: Vacuum, Surfaces, and Films **9** (1), 116-123 (1991).

45. L. Liu, Z. Wang, J. Zhu, Z. Zhang, M. Tan, Q. Huang, R. Chen, J. Xu and L. Chen, Chinese optics letters **6** (5), 384-385 (2008).

46. M. Rubin, C. Hopper, N. Cho and B. Bhushan, Journal of materials Research **5** (11), 2538-2542 (1990).

47. L. Jacobsohn, R. Prioli, F. Freire Jr, G. Mariotto, M. Lacerda and Y.-W. Chung, Diamond and Related Materials **9** (3-6), 680-684 (2000).

48. S. Huebner, N. Miyakawa, A. Pahlke and F. Kreupl, physica status solidi (b) **252** (11), 2564-2573 (2015).

49. S. Huebner, N. Miyakawa, S. Kapser, A. Pahlke and F. Kreupl, IEEE Transactions on Nuclear Science **62** (2), 588-593 (2015).

50. S. Huebner, N. Miyakawa, A. Pahlke and F. Kreupl, MRS Advances **1** (20), 1441-1446 (2016).

51. J. Vlassak and W. Nix, Journal of materials research **7** (12), 3242-3249 (1992).

52. M. K. Small and W. Nix, J. Mater. Res **7** (6) (1992).

53. P. Fallon and L. M. Brown, Diamond and Related Materials **2** (5-7), 1004-1011 (1993).

54. J. Schwan, S. Ulrich, H. Roth, H. Ehrhardt, S. Silva, J. Robertson, R. Samlenski and R. Brenn, Journal of applied physics **79** (3), 1416-1422 (1996).

55. C. Casiraghi, A. Ferrari and J. Robertson, Physical Review B **72** (8), 085401 (2005).

56. F. Fasudhd, presented at the IEEE, Micro Electro Mechanical Systems Workshop, Napa Valley, California, 1990 (unpublished).

57. C. A. Klein and G. F. Cardinale, Diamond and Related Materials **2** (5-7), 918-923 (1993).

58. L. Jacobsohn and F. Freire Jr, Journal of Vacuum Science & Technology A: Vacuum, Surfaces, and Films **17** (5), 2841-2849 (1999).

59. J. Gaspar, M. E. Schmidt, J. Held and O. Paul, Journal of microelectromechanical systems **18** (5), 1062-1076 (2009).

60. J. Beams, The Structure and Properties of Thin Film (1959).

61. Y. Xiang, X. Chen and J. J. Vlassak, Journal of materials research **20** (9), 2360-2370 (2005).

62. X. Wei, D. Lee, S. Shim, X. Chen and J. W. Kysar, Scripta materialia **57** (6), 541-544 (2007).

63. A. Al-Sharadqah and N. Chernov, Electron. J. Statist. **3**, 886-911 (2009).

64. C. Wen-Hsien, T. Luger, R. K. Fettig and R. Ghodssi, Journal of Microelectromechanical Systems **13** (5), 870-879 (2004).

65. K. Suzuki, Y. Matsuki, K. Masaki, M. Sato and M. Kuroda, Materials Science and Engineering: A **513-514**, 77-82 (2009).

66. B. Weiss, V. Gröger, G. Khatibi, A. Kotas, P. Zimprich, R. Stickler and B. Zagar, Sensors and Actuators A: Physical **99** (1), 172-182 (2002).

67. J. Neggers, J. P. Hoefnagels and M. G. Geers, Journal of materials research **27** (9), 1245-1250 (2012).

68. Y. Zhu, S. Murali, W. Cai, X. Li, J. W. Suk, J. R. Potts and R. S. Ruoff, Advanced Materials **22** (35), 3906-3924 (2010).

69. G. H. Lee, R. C. Cooper, S. J. An, S. Lee, A. van der Zande, N. Petrone, A. G. Hammerberg, C. Lee, B. Crawford, W. Oliver, J. W. Kysar and J. Hone, Science **340** (6136), 1073-1076 (2013).

70. H. I. Rasool, C. Ophus, W. S. Klug, A. Zettl and J. K. Gimzewski, Nature communications **4**, 2811 (2013).

71. J. S. Bunch, S. S. Verbridge, J. S. Alden, A. M. van der Zande, J. M. Parpia, H. G. Craighead and P. L. McEuen, Nano letters **8** (8), 2458-2462 (2008).

72. J. W. Suk, A. Kitt, C. W. Magnuson, Y. Hao, S. Ahmed, J. An, A. K. Swan, B. B. Goldberg and R. S. Ruoff, Acs Nano **5** (9), 6916-6924 (2011).

73. Q. Zhou and A. Zettl, Applied Physics Letters **102** (22), 223109 (2013).

74. K. S. Kim, Y. Zhao, H. Jang, S. Y. Lee, J. M. Kim, K. S. Kim, J. H. Ahn, P. Kim, J. Y. Choi and B. H. Hong, Nature **457** (7230), 706-710 (2009).

75. G. Odahara, S. Otani, C. Oshima, M. Suzuki, T. Yasue and T. Koshikawa, Surface Science **605** (11-12), 1095-1098 (2011).

76. R. S. Weatherup, B. C. Bayer, R. Blume, C. Ducati, C. Baehtz, R. Schlögl and S. Hofmann, Nano letters **11** (10), 4154-4160 (2011).

77. R. S. Weatherup, C. Baehtz, B. Dlubak, B. C. Bayer, P. R. Kidambi, R. Blume, R. Schloegl and S. Hofmann, Nano letters **13** (10), 4624-4631 (2013).

78. T. Iwasaki, H. J. Park, M. Konuma, D. S. Lee, J. H. Smet and U. Starke, Nano letters **11** (1), 79-84 (2011).

79. W. Liu, C.-H. Chung, C.-Q. Miao, Y.-J. Wang, B.-Y. Li, L.-Y. Ruan, K. Patel, Y.-J. Park, J. Woo and Y.-H. Xie, Thin Solid Films **518** (6, Supplement 1), S128-S132 (2010).

80. M. Sarno, C. Cirillo, R. Piscitelli and P. Ciambelli, Journal of Molecular Catalysis A: Chemical **366**, 303-314 (2013).

81. R. S. Weatherup, B. Dlubak and S. Hofmann, Acs Nano **6** (11), 9996-10003 (2012).

82. S.-e. Zhu, S. yuan and G. C. A. M. Janssen, EPL (Europhysics Letters) **108** (1), 17007 (2014).

83. E. H. Martins Ferreira, M. V. O. Moutinho, F. Stavale, M. M. Lucchese, R. B. Capaz, C. A. Achete and A. Jorio, Physical Review B **82** (12) (2010).

84. W. C. Fazio, J. M. Lund, T. S. Wood, B. D. Jensen, R. C. Davis and R. R. Vanfleet, presented at the ASME International Mechanical Engineering Congress and Exposition, 2011 (unpublished).

85. R. Negishi, H. Hirano, Y. Ohno, K. Maehashi, K. Matsumoto and Y. Kobayashi, Thin Solid Films **519** (19), 6447-6452 (2011).

86. N. Boyer, L. Pei, J. Rowley, D. Syme, S. Liddiard, J. Abbott, K. Larson, Z. Liang, B. Iverson and R. Vanfleet, Materials Research Express **4** (3), 035032 (2017).